NOVEL QUANTITATIVE MRI ACQUISITION

FOR ACCESSIBLE APPLICATION

by

JEEHUN KIM

Submitted in partial fulfillment of the requirements for the

Degree of Doctor of Philosophy

Electrical Engineering

CASE WESTERN RESERVE UNIVERSITY

August, 2024

CASE WESTERN RESERVE UNIVERSITY
SCHOOL OF GRADUATE STUDIES

We hereby approve the dissertation of

Jeehun Kim

Candidate for the degree of Doctor of Philosophy

Committee Chair

M. Cenk Cavusoglu, Ph.D.

Committee Member

Xiaojuan Li, Ph.D.

Committee Member

Xin Yu, Sc.D.

Committee Member

Mark Griswold, Ph.D.

Date of Defense

July 1, 2024

*We also certify that written approval has been obtained

for any proprietary material contained therein

Table of Contents

List of Tables

List of Figures

Acknowledgements

I would like to express my deepest gratitude to my dissertation supervisor, Dr. Xiaojuan Li, for the wonderful guidance, insightful feedback, and unwavering support throughout my research journey. Her expertise and encouragement have been instrumental in shaping this dissertation.

I am grateful to the members of my dissertation committee, Dr. M. Cenk Cavusoglu, Dr. Xin Yu, Dr. Mark Griswold for their valuable feedback on my research and for their support. Special thanks are also due to the Lerner Research Institute and Mellen Imaging Center for providing essential resources, facilities, and a supportive research environment throughout my doctoral studies.

I would like to acknowledge the collaborators who contributed to this research. Their expertise and dedication were instrumental in the successful completion of this dissertation. In particular, University of California San Francisco, University of Kentucky, Albert Einstein College of Medicine and Montefiore Medical Center, State University of New York at Buffalo, National Institute of Standards and Technology (NIST), and Calimetrix Inc for their collaboration in multiple research projects. I am also grateful to the sponsorship from NIH and the Arthritis Foundation for our research projects.

To my family and friends, I owe a debt of gratitude for their love, encouragement, and understanding throughout this challenging endeavor. Their unwavering belief in me sustained my motivation.

Lastly, I wish to thank Dr. Wanyong Shin for the insightful discussions in both scientific and personal topics.

This work would not have been possible without the support and encouragement of each individual and institution mentioned above. Thank you.

List of Abbreviations

qMRI = Quantitative Magnetic Resonance Imaging

MSK = Musculoskeletal

OA = Osteoarthritis

PG = Proteoglycans

GAG = Glycosaminoglycans

SNR = Signal-to-Noise Ratio

3D = 3-dimensional

2D = 2-dimensional

TI = Inversion Time

TE = Echo Time

TR = Repetition Time

TSL = Time of Spin-Lock

FSL = Spin-Lock Frequency

3D MAPSS = 3D Magnetization-Prepared Angle-Modulated Partitioned K-space Spoiled Gradient-Echo Snapshots

CS = Compressed Sensing

DL = Deep Learning

CV = Coefficient of Variation

MNAD = Median Normalized Absolute Difference

Novel Quantitative MRI Acquisition

for Accessible Application

Abstract

By

JEEHUN KIM

Quantitative Magnetic Resonance Imaging (qMRI) is a powerful tool for detecting biochemical abnormalities without harmful ionizing radiation and invasive procedure, which can significantly enhance early disease diagnosis and progression monitoring compared to standard morphological MRI. Osteoarthritis is a disease significantly impacting joint function, mobility, and quality of life, often leading to chronic pain and reduced physical activity. Despite the significant impact, the disease lacks sensitive biomarker that can detect and track the disease progression from an early stage which can help improve patient outcomes and develop effective treatment for the disease. qMRI, due to its sensitivity to biochemical properties, provide multiple candidates that may serve as imaging biomarkers for OA. Among them, T_2 and $T_{1\rho}$ have advantage of not requiring special coil nor contrast agent. However, challenges need to be addressed to expand the accessibility of the technique and successful translation to be used in large scale clinical trials and in clinical practice.

In this study, novel quantitative T_2 and $T_{1\rho}$ acquisition techniques were developed to enhance reliability and enable faster acquisition.

CHAPTER I: INTRODUCTION

Technological development during the last two centuries had great positive impact on human lifestyle, and advancements in medical field has greatly dedicated in this aspect by helping people live a healthier and happier life. Magnetic resonance imaging (MRI) is certainly an influential invention since it allowed non-invasive imaging of human body without harmful radiation.

Conventional diagnosis using clinical morphological MRI images (e.g. T_1-, T_2-weighted images) is performed by radiologists based on their perception of image contrasts. Combined with the ample amount of anatomical information collected from various images, information of the tissue physiology, and keen eyes of trained radiologists to capture abnormality from the image, MRI was successfully applied to numerous disease diagnosis. However, since the interpretation is based on individual radiologist's decision, the diagnosis is subjective and can vary depending on the experience and expertise of the interpreter. Such subjectivity is detrimental when trying to find a reproducible biomarker for a disease. Furthermore, such qualitative evaluation lacks sensitivity to detect changes that may be challenging for human eyes to discern.

Quantitative MRI, in contrary to the conventional qualitative MRI, denotes the methods that assess MRI images with physical quantitative measurements. Such measurements can be as simple as size of the tumor to fundamental physical properties such as T_1 and T_2. Quantitative MRI offers significant advantages over qualitative MRI. First, due to its quantitative nature, it allows direct comparison of measurements. This facilitates easy processing of images from a large cohort, thereby enabling more consistent

diagnosis criteria compared to qualitative MRI. Additionally, its ability to capture fundamental properties of tissue lead to increased biological specificity and has potential for developing biomarkers for pathophysiological processes that can better detect and track diseases where diagnosis based solely on anatomic information is challenging. Therefore, successful clinical translation of quantitative MRI can significantly improve diagnosis and prognosis and use the MRI technique in its full potentials.

One of the key challenges of quantitative MRI in clinical translation is how to improve reliability of the measurements. In qualitative MRI, subtle changes in image due to system imperfections such as change in signal-to-noise ratio (SNR) may not influence the radiologists' decision, but quantitative MRI can be affected by these changes. Another challenge is longer acquisition times for collecting MRI protocols with different sequence parameters can lead to unfeasible scan times in clinical practice. Therefore, the goal of this study is to address these challenges to develop a quantitative MRI acquisition that can be more accessible in the clinical setup.

CHAPTER II: BACKGROUND INFORMATION

II.1 OSTEOARTHRITIS

Osteoarthritis (OA) is a degenerative disease affecting multiple joint tissues such as cartilage, bone, ligament, tendon and muscle, and characterized by pain, stiffness, and loss of function.[1] The disease is the most common form of synovial joint disorder, affecting 30.8 million adults in the USA.[2] The disease is the leading cause of disability, and healthcare cost for treating OA in the USA is estimated to be $139.8 billion annually.[3] Despite its significant impact, due to lack of sensitive and reliable non-invasive biomarkers, early diagnosis and prognosis of OA remain challenging. Lack of biomarker also hinders development of disease-modifying OA drugs (DMOADs) since it is hard to detect the treatment effects over a short-time window.[4, 5] The standard method for a clinician to determine the stage of OA within a joint is examining image features such as joint space narrowing or formation of osteophytes in radiographs (X-ray images). Although cost effective, radiographs fundamentally lack soft tissue image contrast. Clinical morphological MRI has been used for evaluating joint injury and structural damages, which offers superior soft tissue contrasts and 3D planar imaging. However, both methods lack sensitivity to early stage of OA.

Cartilage damage and degeneration are among hallmark manifestations of OA. Articular cartilage is a tough, flexible connective tissue that protects the joints and bones during movement by decreasing the friction and distributing the load. It consists of a low density of chondrocytes surrounded by a large extracellular matrix primarily composed of water, collagen, and proteoglycans.[6] Water constitutes 65 to 80 percent of total cartilage

mass, and the liquid nature of cartilage allows its load-dependent deformation. 10 to 20 percent of total mass is collagen, primarily consisting of Type II collagen, which provides microfibrillar frame and tensile strength to the cartilage. 10 to 15 percent of total cartilage mass is proteoglycans. Proteoglycans consists of protein core and glycosaminoglycans (GAGs) attached to the protein core. GAGs are highly polar and negatively charged, thus have a strong tendency to attract water molecules and increase osmolarity by attracting positively charged ions such as sodium. Proteoglycans provide compressive strength, and it is known to deplete in the early stage of OA.[6] Therefore, developing imaging methods that are related to these pathological changes is the key to finding biomarkers for early stage of OA.

II.2 QUANTITATIVE MRI METHODS FOR OA

Extensive research has been conducted to identify sensitive biomarkers that can probe the biochemical composition of the cartilage matrix. Methods such as T_2 mapping, $T_{1\rho}$ mapping, delayed gadolinium-enhanced MRI of cartilage (dGEMRIC), diffusion MRI, chemical exchange saturation transfer (gagCEST), and sodium MRI have shown to provide information about the compositional changes in cartilage proteoglycan-collagen matrix known to occur in the early stages of OA.[7, 8] Among the various methods, T_2 have shown to be sensitive to changes in water content, collagen structure and concentrations, while $T_{1\rho}$ have shown to correlate with GAG concentration.[9, 10] The changes in T_2 and $T_{1\rho}$ provided information to distinguish patients with early OA or those who are at risk of developing OA from healthy controls and predict disease progression in OA or acutely injured knees.[11, 12] One of the advantages of using T_2 and $T_{1\rho}$ mapping techniques is they

do not need contrast agent injection or special coil, which can facilitate large scale multi-site multi-vendor trials and promote accessibility. Therefore, this study will focus on developing and improving T_2 and $T_{1\rho}$ mapping techniques. The mapping technique shares the most common challenges of other quantitative MRI techniques: standardization, reliability, and long acquisition time.

II.3 BLOCH EQUATION

The fundamental physics of MRI utilizes the nuclear magnetic resonance (NMR) phenomenon, which states if a non-zero quantum of nuclear spin is placed into an external magnetic field, it will align parallel or anti-parallel to the applied magnetic field. Since a quantum nuclear spin can be approximated to a rotating charge, different alignment of the nuclear spin to the magnetic field results in different energy levels where anti-parallel spins have higher energy, and parallel spins have lower. This difference allows radiative absorption and emission when the nuclear spin changes its energy level. For proton, the spin can have two energy levels, and the difference between the two defines the magnetic resonance frequency of the radiofrequency (RF) electromagnetic radiation. Using this phenomenon, NMR spectroscopy analyzes the absorbed and emitted RF field from the material under large external magnetic field to identify the composition of proteins or other complex molecules.

MRI utilizes the same phenomenon on the abundant protons in human body, hydrogen, but in a slightly different way. On top of modulating the resonance frequency as done in NMR spectroscopy, MRI modulates the resonance frequency according to the position. This is achieved by applying spatially varying magnetic field that has the same

direction as the external magnetic field called gradient magnetic field using gradient coils. The application of gradient magnetic field helps the acquisition of the MRI images by allowing spatial selection during excitation and acquire frequency-encoded image called k-space which the original image can be recovered by Fourier transform.

Although the motion of individual nuclear spin is based on quantum mechanics, motion of the spin in a macroscopic scale can be estimated to a more classical physical model.
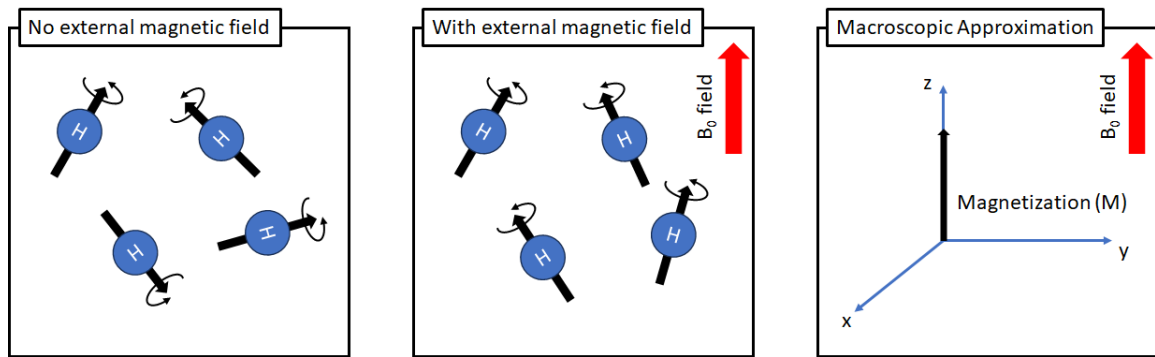
Figure 1 Schematic for the macroscopic approximation of the nuclear spins. The external magnetic field, B_0 field, aligns the spins to the direction of the B_0 field, resulting in a net magnetization in macroscopic viewpoint. z-direction commonly denotes the direction of the B_0 field.

As shown in Figure 1, individual protons can be considered as a magnetic dipole since nuclear spin can be approximated to a rotating charge. Without the presence of external magnetic field, commonly noted as B_0 field, these magnetic dipoles will not align to a single direction due to thermal motion and have zero net magnetization. However, when a B_0 field is applied to these spins, the spins will tend to align with the B_0 field, which can be modeled as a single net magnetization (M) pointing in the direction of the B_0 field.

The size of the net magnetization in the equilibrium state (M_0) will be based on multiple factors including number of protons, thermal motion, and size of the B_0 field.

The motion of net magnetization can be calculated by Bloch equation:

$$\frac{d\boldsymbol{M}(t)}{dt} = \gamma \boldsymbol{M}(t) \times \boldsymbol{B}(t) - \frac{\boldsymbol{M}_\perp(t)}{T_2} - \frac{\boldsymbol{M}_\parallel(t) - M_0}{T_1} \quad (1)$$

Where γ is the gyromagnetic ratio of the nuclei, $\boldsymbol{M}$ is the magnetization vector according to time, $\boldsymbol{B}$ is the magnetic field applied to the magnetization vector, $\boldsymbol{M}_\perp$ is the magnetization perpendicular to the B_0 field, called transverse magnetization, and $M_\parallel$ is the magnetization parallel to the B_0 field, called longitudinal magnetization. Time constant T_1 and T_2 are relaxation time constants for longitudinal and transversal relaxation, accordingly.
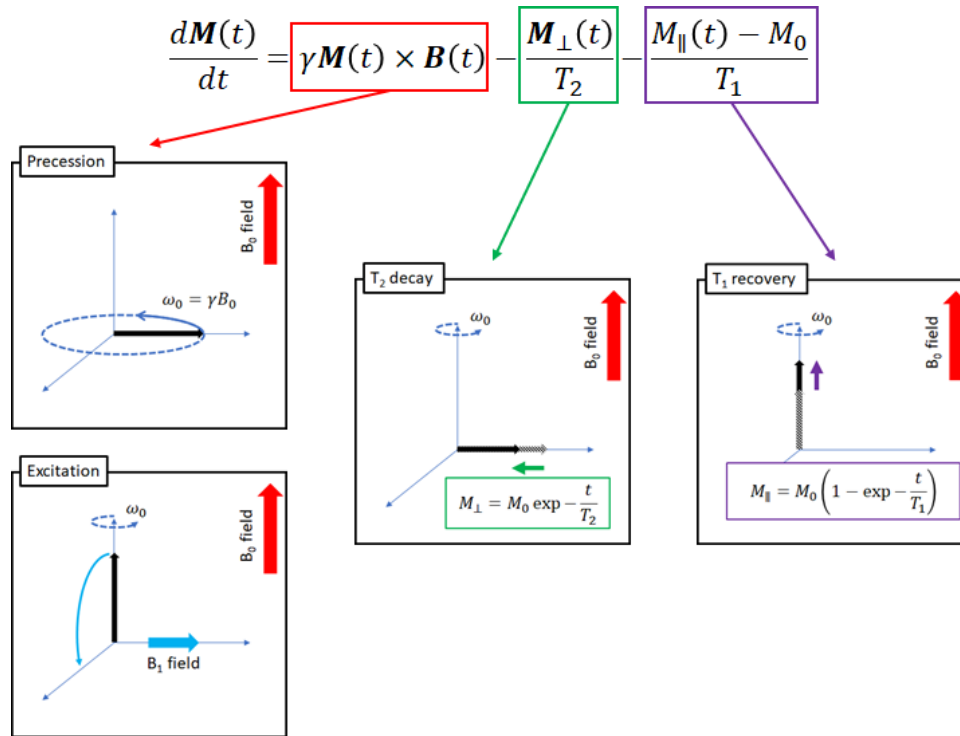
Figure 2 Schematic of the Bloch equation in terms of magnetization.

The three terms in the equation (1) models three different mechanisms, as shown in Figure 2. The first term models the precession of the magnetization perpendicular to applied magnetic field, such as precession of transverse magnetization with regard to B_0

(static field, few T) and RF field (few µT) applied perpendicular to the B_0 field, called B_1 field. When B_1 field is applied in resonant frequency defined by the B_0 field and gyromagnetic constant, called Larmor frequency, the magnetization can be nutated from its original longitudinal direction to transverse plane (called "excited") and precess in Larmor frequency. The second term models the exponential decay of the transverse magnetization in T_2 time constant. After the B_1 field, the excited magnetization will keep precessing until the transverse magnetization decays to 0 (T_2 decay). Commonly T_2 can be quantified by collecting multiple images with different time after excitation (echo time, TE) and applying exponential fitting. And the third term models exponential recovery of the longitudinal magnetization in T_1 time constant. To quantify T_1, images are collected after inversion RF pulse was applied. The time after the inversion pulse is called inversion time (TI), and T_1 can be calculated by combining images with different inversion times.

In an MRI scan, the signal is collected using the RF field created by precessing transversal magnetization using an RF coil. MRI scan can create different image contrasts by changing parameters such as the size of the RF field, time for T_1 recovery, and time of signal acquisition after the RF field, and during the process this equation can be used to model and simulate the signal evolution for a given MRI scan parameters.

II.4 RELAXATION TIME IN THE ROTATING FRAME

$T_{1\rho}$ and $T_{2\rho}$ are relaxation time constants during a special experiment called spin-lock preparation. Compared to T_1 relaxation time that probes the molecular interaction in the range of Larmor frequency of the scanner (e.g. 128 MHz for 3T MRI), $T_{1\rho}$ contains the information about T1 relaxation times at lower field strength (the strength of spin-lock field,

normally hundreds or thousands Hz), thus helping to capture molecular interaction at a lower frequency.
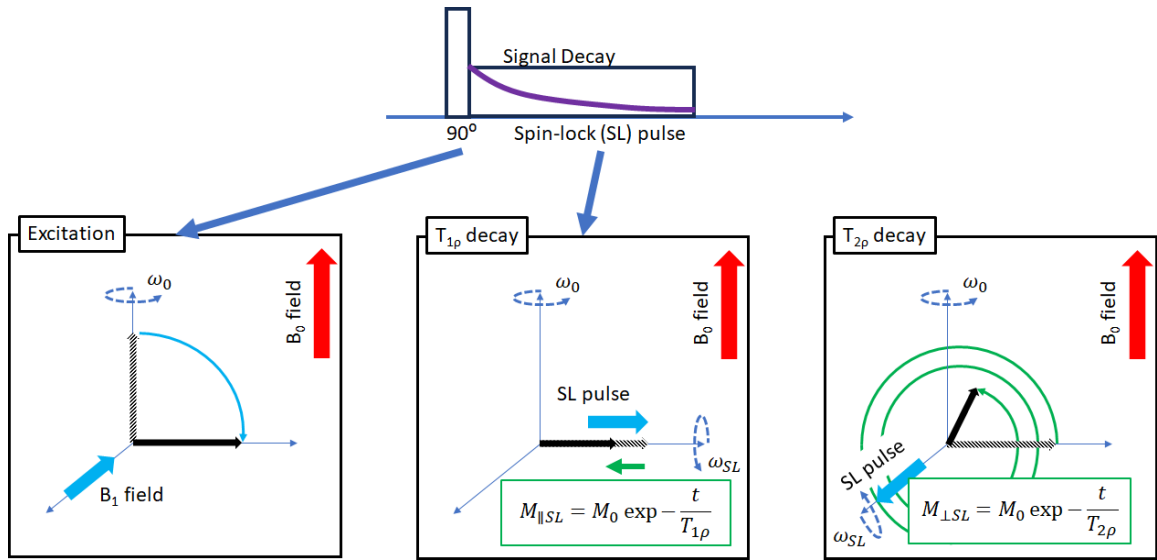
Figure 3 Schematic of spin-lock experiment for $T_{1\rho}$ and $T_{2\rho}$ quantification.

Figure 3 shows the how the spin-lock pulses are applied to the magnetization. First, the magnetization is excited to the transverse plane, and depending on whether its $T_{1\rho}$ and $T_{2\rho}$ quantification, the spin-lock pulse is applied parallel ($T_{1\rho}$) or perpendicular ($T_{2\rho}$) to the magnetization. As the term spin-lock implies, the spin-lock pulse locks the magnetization to the direction of the spin-lock by continuously precessing the magnetization and prevent the directions of magnetization to disperse. In addition to the relaxation of the transverse magnetization, T_2, the spin-lock pulse further slows down the relaxation by the effect of the spin-lock pulse that is parallel to the magnetization. This effect is analogous to the T_1 recovery of longitudinal magnetization due to the B_0 field parallel to the longitudinal magnetization. For this reason, the relaxation time is named as $T_{1\rho}$ although the relaxation happens in the transverse plane. For $T_{2\rho}$ relaxation, the magnetization is constantly precessed to the longitudinal and transverse plane, and this results in much slower relaxation compared to T_2 and $T_{1\rho}$. Therefore, $T_{1\rho}$ is longer or equivalent to T_2, and $T_{2\rho}$ is

longer than $T_{1\rho}$. Important parameters for $T_{1\rho}$ and $T_{2\rho}$ experiments are spin-lock frequency (SLF), magnitude of the spin-lock pulse in Hz (e.g. 500 Hz for typical knee experiment), and time of spin-lock (TSL), the length of the spin-lock pulse which is used to fit $T_{1\rho}$ and $T_{2\rho}$ relaxation times.

II.5 3D MAGNETIZATION-PREPARED ANGLE-MODULATED PARTITIONED K-SPACE SPOILED GRADIENT-ECHO SNAPSHOTS (3D MAPSS)

Collecting $T_{1\rho}$ and T_2 mapping in knee needs two considerations. First, the collection of the $T_{1\rho}$- and T_2-weighted signal should be efficient. Since calculating $T_{1\rho}$ and T_2 map requires multiple $T_{1\rho}$- and T_2-weighted images with different magnetization preparations (e.g. different TSLs for $T_{1\rho}$, TEs for T_2), collecting one line of k-space after magnetization preparation could lead to unfeasible scan time. Therefore, multiple k-space lines should be collected after the magnetization preparation in center-out ordering to preserve the $T_{1\rho}$- or T_2-weighted contrast and speed up the acquisition. Second, the subsequent non-uniform weighting of the k-space coming from acquiring multiple lines after magnetization preparation should be minimized. Average cartilage thickness of normal knee joints ranges from 2 to 3 mm, and for such thin structure the blurring and edge enhancement resulting from non-uniform k-space weighting can deter the sensitivity of the quantification greatly. 3D magnetization-prepared angle-modulated partitioned k-space spoiled gradient-echo snapshots (3D MAPSS) was designed to solve the previous problems.[13, 14]

I. Magnetization preparation (mag prep)				II. Image acquisition
A. Magnetization Reset	Deadtime	B. Fat-selective Inversion	C. T1ρ or T2 Preparation	D. Single k-space Segment

Magnetization Preparation
T1ρ: continuous hard pulse
T2: MLEV train of refocusing pulses ($90_x180_y90_x$)

RF Cycling
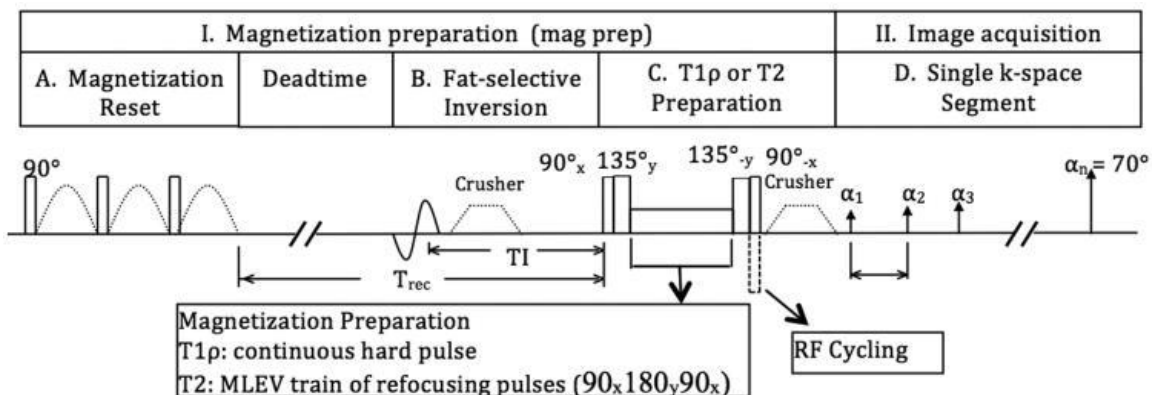
Figure 4 Pulse sequence diagram of 3D MAPSS sequence with T_2 or $T_{1\rho}$ preparations (Li et al., Journal of Magnetic Resonance Imaging, 2014)

Figure 4 shows the pulse sequence diagram of 3D MAPSS sequence. At the start of each acquisition, magnetization reset (Figure 4-A) is applied, followed by T_1 recovery time (Figure 4-Deadtime), to make the starting magnetization equivalent between all acquisitions. Afterwards, fat saturation pulse (Figure 4-B) is applied in advance to the magnetization preparation to remove the unwanted fat signal from being acquired. After the T_2 or $T_{1\rho}$ preparation pulse (Figure 4-C) is applied, multiple k-space lines are acquired in a center-out manner (Figure 4-D) to efficiently collect data and preserve the contrast created by the magnetization preparation as much as possible. To mitigate the unwanted non-uniform k-space weighting during this process, RF cycling along with the variable flip angle acquisition is applied.

If we define the transverse magnetization after n-th excitation pulse $M_{xy}(n)$, it can be described as,

$$M_{xy}(n) = A(n)M_{prep} + B(n)$$

Where M_{prep} is the longitudinal magnetization after the T_2 or $T_{1\rho}$ preparation pulse, $A(n)$ is a term containing the T_1 decay of the prepared longitudinal magnetization over time, and

$B(n)$ is a term containing the T_1 recovery of the longitudinal magnetization. Both $A(n)$ and $B(n)$ are independent of M_{prep}, so to acquire a flat signal during the consecutive acquisition (constant $M_{xy}(n)$ regarding n), size of M_{prep} should be considered during the calculation of excitation flip angle, which results in different flip angle train with different preparation (e.g. TSL, TE), and could lead to quantification errors when assumptions does not conform to the actual acquisition. Therefore, the method introduces RF cycling, which means at the end of the preparation you acquire one acquisition after flipping the magnetization to +z direction (parallel to B₀) and another acquisition after flipping the magnetization to -z direction (anti-parallel to B₀). In this way, the two acquisitions have a signal equation of,

$$M_{xy}^+(n) = A(n)M_{prep} + B(n)$$

$$M_{xy}^-(n) = A(n)\left(-M_{prep}\right) + B(n)$$

Where M_{xy}^+ and M_{xy}^- denotes the flip up and flip down acquisition (Figure 4-C), and the difference of the two eliminates the term $B(n)$,

$$M_{xy,combined}(n) = M_{xy}^+(n) - M_{xy}^-(n) = 2A(n)M_{prep}$$

And the constant $M_{xy}(n)$ regarding n can be achieved by solving the flip angle train that achieves constant $A(n)$ regarding n, and this flip angle train can be used regardless of the size of M_{prep}. Throughout the study, 3D MAPSS sequence was used for data acquisition.

II.6 STUDY OUTLINE

The goal of this study is to develop a quantitative MRI acquisition with improved reliability and faster acquisition time so that it can be more accessible in the clinical setup. First, the current status of reliability of T_2 and $T_{1\rho}$ quantification was evaluated in a multi-vendor multi-site setup in terms of intra-site repeatability and inter-site reproducibility in Chapter III. Second, B_1 and B_0 robust $T_{1\rho}$ preparation was designed and evaluated using Bloch equation-based numerical simulation and actual acquisitions in phantom and in-vivo volunteers in Chapter IV. Third, musculoskeletal (MSK) research-dedicated relaxometry phantom was developed and evaluated using MRI and NMR acquisitions in Chapter V. Lastly, advanced accelerated reconstruction methods using Compressed Sensing (CS) and Deep Learning (DL) was implemented and evaluated in volunteer scans with and without pathology in Chapter VI, and final conclusion will be made in Chapter VII.

CHAPTER III: MULTI-VENDOR MULTI-SITE T1ρ AND T2 QUANTIFICATION OF KNEE CARTILAGE

III.1 INTRODUCTION

As explained in Chapter I, reliability of the quantification is crucial for qMRI since the diagnosis is directly affected by the quantified number. $T_{1\rho}$ and T_2 values have been evaluated in terms of repeatability in single-site studies[15-20] and reproducibility in multi-site studies with a single vendor (average CV of 4.9% for $T_{1\rho}$ and 3.3-6.5% for T_2),[14, 21, 22] but few studies have examined the reliability in a multi-site, multi-vendor context. Only one study has reported inter-vendor reliability of T_2 with mean differences of 5.4-10.0ms (10-25%).[22] Understanding and documenting these variations is critical for large-scale multi-vendor multi-site clinical trials using $T_{1\rho}$ and T_2 imaging.

It is also well known that measured $T_{1\rho}$ and T_2 values are dependent on MRI pulse sequences.[23-25] Although T_2 imaging based on multi-echo spin-echo acquisition is available as product sequences on most MR systems, differences in implementation details between vendors are unknown, and the T_2 values derived from this sequence are known to be susceptible to B_1 inhomogeneity-invoked stimulated echoes.[26] Since $T_{1\rho}$ imaging is only available as research prototypes on MR systems, published $T_{1\rho}$ studies have used sequences with different structures (balanced or non-balanced gradient-echo vs spin-echo readout, variable flip angle vs constant flip angle, with and without RF cycling, etc.) on different MR systems.[13, 27, 28] To date, no $T_{1\rho}$ imaging acquisition with similar sequence structure is available across the different vendors' MR systems. Acquisition of $T_{1\rho}$ and T_2 using the exact same readout will facilitate comparisons of these two measures, as well as

exploration of interesting new markers such as $R_2 - R_{1\rho}$ (a composite relaxation rate created to describe extracellular matrix using a single metric).[29]

The goals of this chapter were to: 1) implement $T_{1\rho}$ and T_2 mapping using the same sequence structure at 3T on three vendor platforms (Siemens, GE, Philips) located at four geographically different sites; 2) standardize imaging protocols and data processing procedures; and 3) measure intra-site repeatability and inter-site reproducibility of $T_{1\rho}$ and T_2 measures in phantoms and human volunteers.

III.2 METHODS

III.2.1 Acquisition Setup

Phantoms and volunteers were scanned at four sites using 3T MRI systems from three vendors to evaluate intra- and inter-site variability (Table 1). The phantoms consisted of six tubes with three different agarose concentrations (2, 3, and 4%, weight/volume) fixed in a cylinder holder (manufactured by the Phantom Lab), each scanned three times in three different positions. Five knees from volunteers were scanned in feet-first supine position at each site after informed consent, including three knees from two traveling volunteers who were scanned at all four sites. All procedures were approved by the Institutional Review Board (IRB) at all participating sites. All volunteers were required to sit for at least 30 minutes before scans to equilibrate loading status to knee cartilage.

a) MR systems and RF coils				
	Site 1	Site 2	Site 3	Site 4
MR system	Siemens Prisma	Siemens Prisma	GE Discovery™ MR750 wide bore	Philips Ingenia wide bore
Software	VE11C	VE11C	DV25R2	5.3.1
RF coil	QED 1Tx/15Rx knee coil	QED 1Tx/15Rx knee coil	Invivo 1Tx/8Rx knee coil	Invivo 1Tx/16Rx coil

b) $T_{1\rho}$ and T_2 imaging		
	Phantom	**Volunteer**
FOV	140x140x80 mm^3	140x140x96 mm^3
Imaging matrix	256x128x20	320x160x24
Image orientation	Transversal	Sagittal
Time of recovery	1.5 seconds	
Number of echoes	8	
Bandwidth per pixel (Hz)	400 Hz	
Views per segment	76 (Site 1, 3, 4) 128 (Site 2)	92 (Site 1, 3, 4) 160 (Site 2)
Parallel imaging	Factor 2 (Site 1, 3, 4) None (Site 2)	Factor 2 (Site 1, 3) Factor 1.6×1.6 (Site 4) None (Site 2)
Time of Spin-Lock (TSL)	0, 10, 20, 30, 40, 50, 60, 70 ms	
Spin-Lock Frequency	500 Hz	
T_2 preparation TE	0, 9.7, 21.3, 32.9, 44.5, 56.1, 67.6, 79.2 ms (Site 1) 5, 10, 20, 30, 40, 50, 60, 70 ms (Site 2) 0, 8.8, 17.7, 26.5, 35.4, 44.2, 53.1, 61.9 ms (Site 3) 0, 6.83, 15.3, 23.7, 32.1, 40.6, 49.0, 57.4 ms (Site 4)	
Acquisition time	10:40 (Site 1) 6:24 (Site 2) 10:41(Site 3) 9:04 (Site 4)	13:43 (Site 1) 7:48 (Site 2) 14:42(Site 3) 9:11 (Site 4)

c) List of scan parameters used to evaluate scan parameter dependency	
$T_{1\rho}$ imaging	Combinations of time of recovery (0.8, 1.5, and 3 seconds), views per segment (64 and 128), with and without parallel imaging
T_2 imaging	TE_set1 = [1.86 8.59 17.18 25.78 34.37 42.96 51.55 60.14] ms TE_set2 = [1.86 9.99 19.98 29.98 39.97 49.96 59.95 69.94] ms TE_set3 = [1.86 11.59 23.18 34.78 46.37 57.96 69.55 81.14] ms

d) High-resolution gradient echo imaging				
	Site 1 (DESS)	Site 2 (DESS)	Site 3 (SPGR)	Site 4 (FFE)
FOV (mm^3)	140x140x112	140x140x112	140x140x114	140x140x112
Imaging matrix	384x307x160	256x238x160	384x300x114	388x310x160
TR (ms)	17.55	17.55	13.036	18
TE (ms)	6.02	6.02	2.716	6.5
Flip angle (°)	25	25	25	25
Bandwidth per pixel (Hz)	185	240	139	185

Table 1 Hardware information and imaging parameters for data collection

III.2.2 Phantom Evaluation

The $T_{1\rho}$ and T_2 sequence protocols were imaged at three different coil locations (left 70mm, center, and right 70mm) to evaluate the effect of knee laterality. At each site, phantoms were imaged three times on different days within a week. Phantoms were kept in the scanner room at least overnight before each scan and the room temperature was recorded. Phantom orientation inside the coil was the same for all sites. Table 1b lists the parameters used for phantom imaging. Each site used the minimum allowed TR and TE. The acquisition parameter dependence of 3D MAPSS was investigated at Site 1 by evaluating $T_{1\rho}$ and T_2 reproducibility with sequence parameters changes (Table 1c).

III.2.3 Volunteer Evaluation

In addition to $T_{1\rho}$ and T_2 imaging, a high-resolution gradient echo (GRE) imaging (spoiled gradient-echo [SPGR] for GE, T1 fast field echo [T1-FFE] for Philips, and dual-echo steady-state [DESS] for Siemens) was performed for cartilage segmentation. All scans were performed with fat suppression using frequency selective excitation, followed by crusher gradient. The parameters for each site are listed in Table 1d. All volunteers were repositioned in the magnet between scan and rescan acquisitions.

III.2.4 Image Processing

Phantom: An automatic segmentation method was used to select the region of interest (ROI) for each tube by removing the background, finding six connected components, and eroding 10 pixels in the periphery to avoid edge artifact.

Volunteers: A standardized workflow was established for robust image registration to ensure efficient and objective intra- and inter-site comparison of images as diagrammed in Figure . Detailed descriptions are listed below.

a) Each volunteer dataset consisted of high-resolution GRE, $T_{1\rho}$, and T_2 images. All images within a dataset were registered to the first echo of the $T_{1\rho}$ images, using Elastix's rigid registration.[30] A mask covering the areas surrounding the patella, tibia, fibula, and femur, generated by warping a predefined mask on a template image, was used in Elastix to guide the registration. The template image was generated by averaging images from the Osteoarthritis Initiative (OAI) dataset.

b) The intra-site rescan images were nonlinearly registered to the initial scan images using ANTS[31] by registering the first echo of $T_{1\rho}$ and high-resolution GRE images simultaneously. Registration was evaluated for subtle shifts visually by switching between different images. The resulting nonlinear transformation was then applied to the other rescan images for the subject. The cartilage ROIs were nonlinearly warped to the rescan images.

c) For inter-site comparison, each traveling subject's images across the four sites were registered to the scan of that subject acquired at Site 1, using the same method as in b).
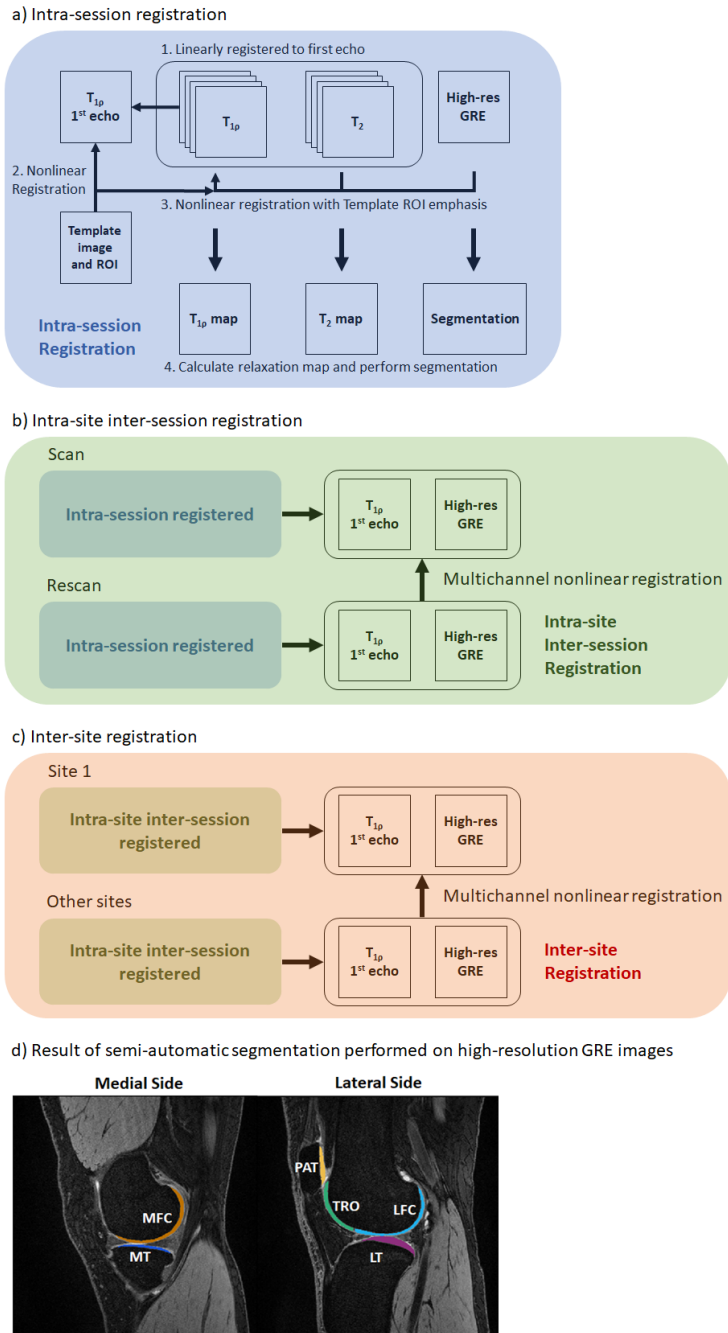
Figure 5 a, b, c) Flowchart of image registrations performed on volunteer data. For intra-site evaluation, segmentation was performed on the high-resolution GRE image of the first scan. For inter-site evaluation, segmentation was performed only on the first scan high-resolution GRE from Site 1. d) Example segmentation map on registered high-resolution GRE image.

Cartilage compartments, including medial/lateral femur (MFC/LFC), medial/lateral tibial (MT/LT), trochlear (TRO), and patella (PAT), were segmented using a custom graphical image interface and adjusting control points on b-spline curves (Figure d). The segmentation was based on the registered high-resolution GRE image, which was guided by gradient image as the reader selected control points around the cartilage region, making the process semi-automatic. To confirm the reproducibility of segmentation, the primary and another trained segmenter independently segmented a total of 24 compartments from four knees. The inter-segmenter CVs for $T_{1\rho}$ and T_2 were 1.17% and 1.38%, respectively, indicating small inter-observer variation. For traveling volunteers, the cartilage segmentation was performed once on the registered high-resolution GRE image from Site 1. Following registration and segmentation, statistical measures for each cartilage compartment were computed after a mono-exponential fitting of the registered $T_{1\rho}$, and T_2 images.

III.2.5 Relaxation time fitting

A voxel-wise two parameter mono-exponential fitting was performed to calculate T2 and T1ρ, based on the Levenberg-Marquardt algorithm using MATLAB (MathWorks, Natick, MA) with linear regression solution using logarithmic transformation for the initial guess. After relaxation time maps were calculated, the mean and standard deviation (SD) of relaxation times of ROIs, each tube for phantom data and cartilage compartment for volunteer data were calculated. To evaluate the feasibility of using fewer echoes, maps fitted using 4 of the 8 echoes in phantom and volunteer data from Site 1, were created using

two different sets of echoes representing strategies with equal/unequal spaces between echoes (Echo_set1 = [1,3,5,7], Echo_set2 = [1,2,4,8]).

III.2.6 SNR Efficiency Estimation

SNR efficiency was calculated as follows:

SNR efficiency of site n

$$= \frac{\text{Mean instensity of first echo}}{\text{Standard deviation of background}} \times \sqrt{\frac{\text{Acquisition time of Site 1}}{\text{Acquisition time of Site n}}}$$

The ratio of the acquisition time at each site with respect to the acquisition time of Site 1 was used for calculation. For volunteer images, a low signal area in the fat-suppressed bone marrow was used, because background signal was filtered out by one vendor.

III.2.7 Statistical Analysis

CVs were calculated to evaluate variability in phantoms from changing scan parameters. CVs were combined by averaging in both phantoms and volunteers. CVs and intraclass correlation coefficients (ICC) were calculated to investigate intra- and inter-site correlation between sites. ICC(2,1) was calculated for intra-site repeatability and ICC(4,1) was calculated for inter-site reproducibility. The inter-site ICCs and CVs were calculated using data from all sites, and only data from three sites that used 3D MAPSS (Site 1, 3, and 4). Bland-Altman analysis was conducted for volunteer data, and the concordance correlation coefficient (CCC) was calculated between sites for inter-site reproducibility.

III.3 RESULTS

III.3.1 Scan Parameter Dependency of $T_{1\rho}$ and T_2 measures using MAPSS sequences

The MAPSS $T_{1\rho}$ sequence yielded consistent relaxation time measures from the experiments, regardless of differences in time of recovery or views per segment, with and without parallel imaging reconstruction (Figure 6, average CV 0.4%). The differences in T2 measures with different T2 preparation TEs were subtle (average CV 1.02%).
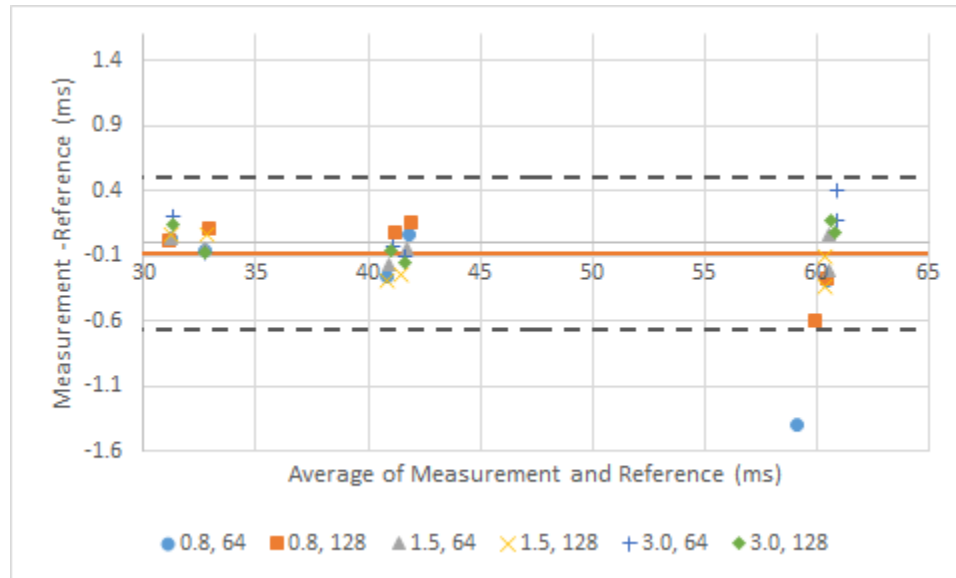
Figure 6 Bland-Altman plots of sequence evaluation with different scan parameters. a) $T_{1\rho}$ measurement with different pairs of time of recovery (seconds) and views per segments. Reference value was measured with the phantom scan protocols which used 1.5 seconds time of recovery and 76 views per segments with GRAPPA 2 reconstruction. b) T_2 measurement with different sequences of T_2 preparation TEs. The sequences of preparation TEs are listed in the methods.

III.3.2 Phantom Evaluation

Figure 7a shows the photo of the phantom. Figure 7b demonstrates phantom measures from each site. $T_{1\rho}$ values were higher than T_2 values, as expected, using MAPSS acquisitions (Site 1, 3 and 4), while T_2 values were higher than $T_{1\rho}$ values, using segmented GRE acquisitions (Site 2). Figure 7c shows the scatter plot of the relaxation time values of all sites with respect to values from Site 1. While no position-related systematic differences were found ($T_{1\rho}$ and T_2 CV (%) = 0.50 and 0.92 for Site 1, 2.59 and 2.11 for Site 2, 1.98 and 2.98 for Site 4), $T_{1\rho}$ for Site 4 showed higher value when positioned in the center. Data from Site 3 had to be excluded due to incomplete data.
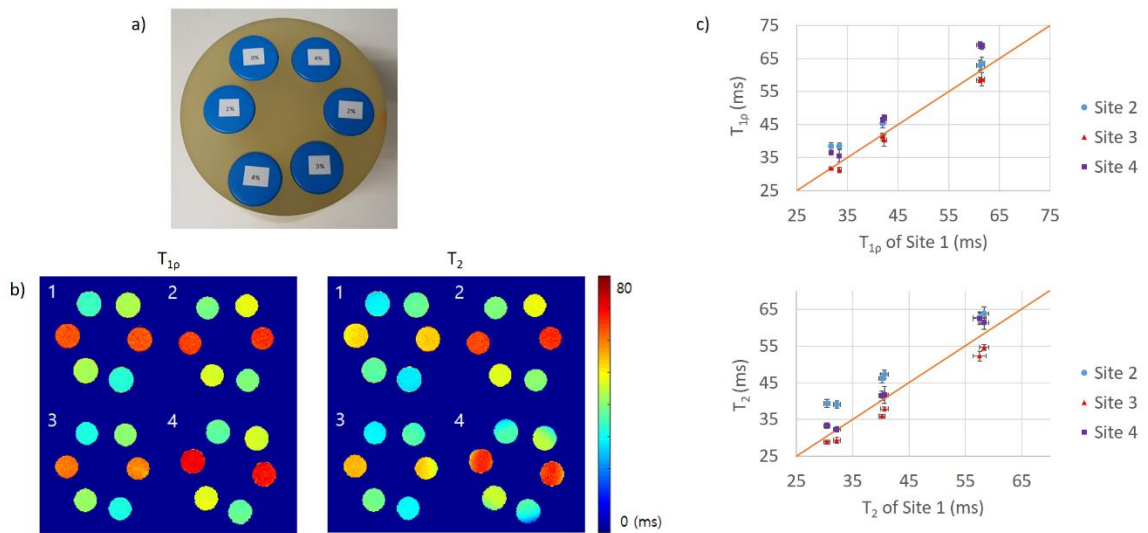
Figure 7 a) Photo of phantom used in this study. b) Example phantom $T_{1\rho}$ and b) T_2 relaxation time maps from all sites. The number in the top left corners of the maps indicates the site. c) Graph of $T_{1\rho}$ and T_2 of each site with respect to the value from Site 1. The diagonal red line shows the reference line of X = Y.

Excellent intra-site repeatability was observed for all sites, with average CVs ranging from 1.09 to 3.05% for $T_{1\rho}$ and from 1.78 to 3.30% for T_2 (Table 2a; measurements

from different coil locations were considered separately when calculating the CVs). Average inter-site CVs for all four sites were 6.54% and 8.44% for $T_{1\rho}$ and T_2, respectively (Table 2b). The average inter-site CVs fell to 6.45% and 5.23% for $T_{1\rho}$, and T_2 respectively when the CV was calculated for data collected by 3D MAPSS only (Site 1, 3, and 4). Between sites, MAPSS relaxation times were highly correlated: ICC of 0.925 (95% CI [0.438, 0.990]) for $T_{1\rho}$ and 0.939 (95% CI [0.492, 0.992]) for T_2. The temperature of the scanner rooms was 20.7°C (Site 1), 17.8°C (Site 2), 22.2°C (Site 3), and 20°C (Site 4).

SNR efficiency varied, ranging from 150 to 227 (Table 2c). All CVs between the phantom relaxation times fitted with 8 echoes and two sets of 4 echoes were smaller than 0.5%.

a)	Average relaxation time $\pm$ SD (ms) (above) and intra-site CV (%) (below) calculated for phantom $T_{1\rho}$ and T_2 measurements						
$T_{1\rho}$	2%-1	2%-2	3%-1	3%-2	4%-1	4%-2	Average
Site 1	61.23±0.74 1.22	61.53±0.55 0.90	41.94±0.42 1.01	42.26±0.44 1.04	33.41±0.37 1.12	31.76±0.39 1.23	1.09
Site 2	62.96±1.52 2.18	63.57±1.84 2.60	45.44±1.39 2.80	46.69±1.22 2.41	38.39±0.98 2.36	38.41±1.17 2.82	2.53
Site 3	58.48±1.02 1.75	58.8±2.43 4.14	41.34±1.25 3.03	40.32±2.18 5.42	31.3±1.04 3.31	31.76±0.21 0.67	3.05
Site 4	69.11±1.03 1.50	68.74±0.95 1.39	46.31±0.77 1.66	47.05±0.59 1.25	35.59±1.9 5.34	36.49±0.45 1.23	2.06
T_2	2%-1	2%-2	3%-1	3%-2	4%-1	4%-2	Average
Site 1	57.55±1.24 2.15	58.33±0.87 1.48	40.22±0.56 1.40	40.65±0.72 1.77	32.21±0.66 2.03	30.47±0.56 1.83	1.78
Site 2	62.78±1.63 2.59	63.81±1.9 2.97	46.2±1.38 3.00	47.24±1.24 2.63	39.09±0.99 2.54	39.36±1.23 3.12	2.81
Site 3	52.26±1.61 3.08	54.62±0.95 1.75	35.88±0.47 1.31	37.87±0.69 1.81	29.37±1 3.40	28.88±0.6 2.08	2.24
Site 4	62.46±1.7 2.72	61.33±1.96 3.20	41.48±1.35 3.25	41.67±2.38 5.72	32.31±0.77 2.39	33.34±0.85 2.55	3.30
b)	Inter-site CV (%) calculated for phantom $T_{1\rho}$ and T_2 measurements						
$T_{1\rho}$	2%-1	2%-2	3%-1	3%-2	4%-1	4%-2	Average
All	6.09	5.71	5.13	6.17	7.55	8.57	6.54
MAPSS	7.05	6.59	5.49	6.53	5.87	7.19	6.45
T_2	2%-1	2%-2	3%-1	3%-2	4%-1	4%-2	Average
All	6.33	5.47	8.10	8.32	10.50	11.94	8.44
MAPSS	6.61	4.62	5.23	5.01	3.96	5.93	5.23

Table 2 Results for phantom $T_{1\rho}$ and T_2 measurements. All: using data from all four sites. MAPSS: using data from sites 1,3,4 that were collected with the MAPSS sequence.

III.3.3 Volunteer Evaluation

Excellent intra-site repeatability for cartilage relaxation times for volunteers was observed at all sites, with average CVs ranging from 1.60 to 3.93% for $T_{1\rho}$ and from 1.44 to 4.08% for T_2 (Table 3a). However, the average inter-site CVs were 13.61% and 20.34% for $T_{1\rho}$ and T_2, respectively (Table 3b). The inter-site CVs were reduced to 8.14% and 10.06% for $T_{1\rho}$ and T_2, respectively, when the data compared were restricted to MAPSS sites only. Figure 8 shows example relaxation maps for one of the traveling volunteers. Both $T_{1\rho}$ and T_2 values were higher at Site 2 than those from other sites. The first traveling volunteer was not scanned at Site 2.

a) Average relaxation time $\pm$ SD (ms) (above) and intra-site CV (%) (below) calculated for volunteer $T_{1\rho}$ and T_2 measurements							
$T_{1\rho}$	LFC	MFC	LT	MT	TRO	PAT	Average
Site 1	49.02±4.65 1.27	43.81±4.79 2.78	46.86±2.55 2.70	42.04±6.79 5.09	47.06±4.59 1.56	44.78±2.45 4.15	2.93
Site 2	57.75±2.31 1.13	52.35±5 0.92	59.35±1.02 0.82	53.67±3.04 1.73	63.08±4.05 2.59	62.7±5.22 2.40	1.60
Site 3	44.92±4.33 2.44	41.74±3.21 2.42	43.32±3.98 2.62	38.45±5.18 0.63	45.48±4.72 3.45	42.81±5 0.91	2.08
Site 4	41.88±2.04 2.32	38.5±3.44 4.87	40.5±2.44 2.87	37.14±4.3 2.75	45.07±3.75 4.47	44.47±4.83 6.32	3.93
T_2	LFC	MFC	LT	MT	TRO	PAT	Average
Site 1	38.88±4.85 1.14	35.04±6.43 3.74	34.77±4.11 2.36	32.59±6.65 6.13	32.7±6.95 4.03	28.95±5.95 7.06	4.08
Site 2	52.3±2.95 0.93	47.35±4.81 1.26	54.91±4.17 1.48	47.66±4.06 0.77	54.06±3.1 2.21	51.36±6.25 1.99	1.44
Site 3	35.14±3.87 3.01	32.49±3.81 4.13	33.13±3.69 2.35	29.44±5.19 1.87	32.38±2.92 2.04	30.5±3.3 2.03	2.57
Site 4	36.67±3.34 2.50	31.93±4.02 4.27	34.18±3.06 0.83	30.37±5.75 1.59	37.3±1.86 2.38	34.84±4.36 1.59	2.20
b) Inter-site CV (%) calculated for volunteer $T_{1\rho}$ and T_2 measurements							
$T_{1\rho}$	LFC	MFC	LT	MT	TRO	PAT	Average
All	9.87	12.35	12.74	11.82	17.12	17.78	13.61
MAPSS	6.36	8.79	7.33	7.33	9.17	9.85	8.14
T_2	LFC	MFC	LT	MT	TRO	PAT	Average
All	15.49	18.35	19.68	18.54	23.15	26.84	20.34

| MAPSS | 5.96 | 8.37 | 9.03 | 9.54 | 10.56 | 16.87 | 10.06 |

c) SNR efficiency of first and last echo of volunteer measurements				
	Site 1	Site 2	Site 3	Site 4
First echo	33.82$\pm$4.74	31.92$\pm$3.23	23.81$\pm$4.99	33.83$\pm$5.55
Last echo ($T_{1\rho}$)	7.25$\pm$0.81	10.24$\pm$1.29	4.88$\pm$0.64	5.16$\pm$0.87
Last echo (T_2)	6.53$\pm$1.52	10.51$\pm$0.87	6.46$\pm$0.91	5.89$\pm$0.84

Table 3 Results for volunteer $T_{1\rho}$ and T_2 measurements. All: using data from all four sites. MAPSS: using data from sites 1, 3, 4 that were collected with the MAPSS sequence.
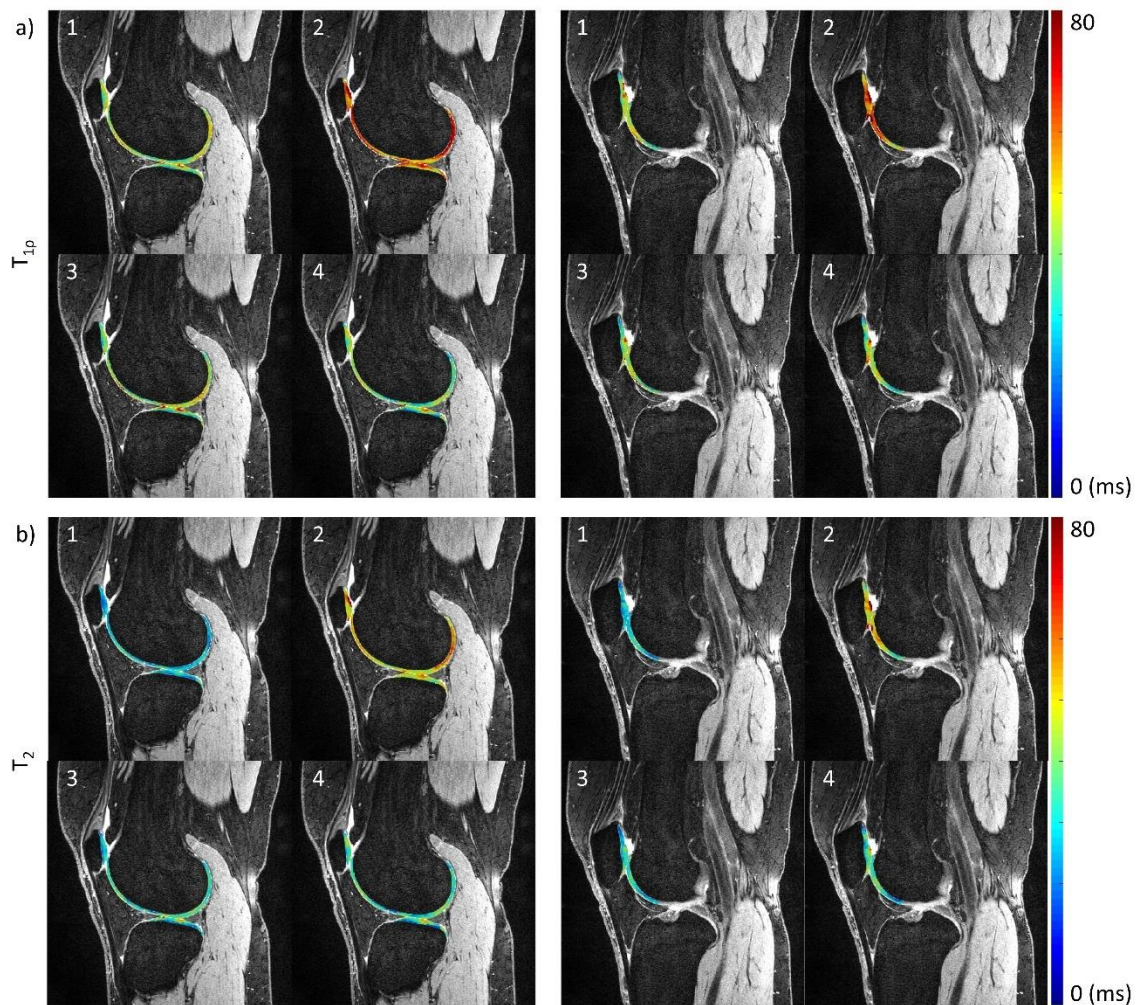
Figure 8 Example volunteer a) $T_{1\rho}$ and b) T_2 relaxation time maps from all sites, overlaid on DESS image from Site 1. The columns show different slice positions. The number on the top left of the images indicates the site.
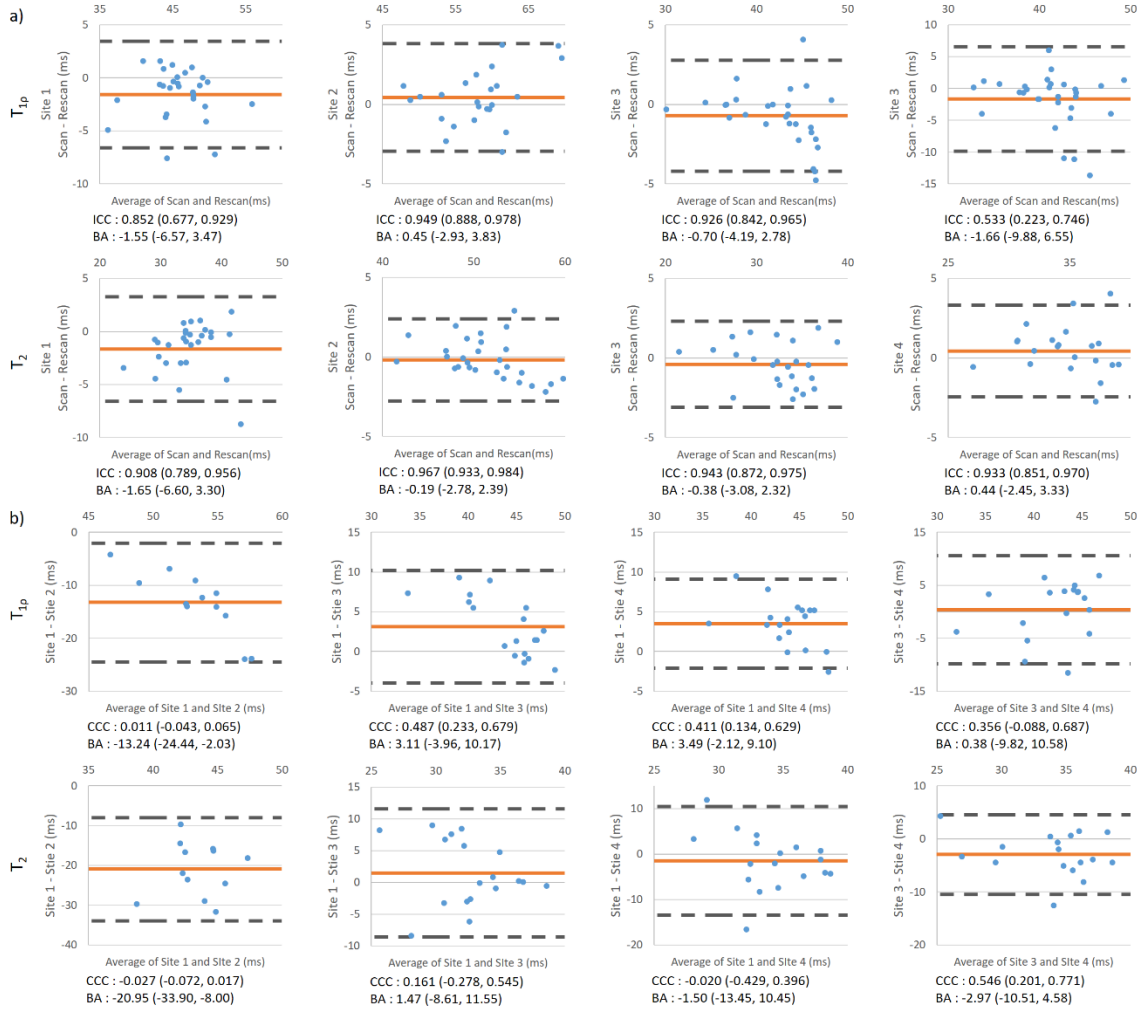
Figure 9 Bland-Altman analysis for (a) intra-site and (b) inter-site $T_{1\rho}$ and T_2. Red line indicates the average of the difference value; dashed black line indicates the upper and lower limit of agreement (LOA). ICCs for intra-site repeatability and CCCs for inter-site reproducibility are listed below each plot. Values in the brackets are 95% confidence intervals. Mean difference and 95% limit of agreement were also listed.

Figure 9 shows the Bland-Altman analysis, ICCs for intra-site repeatability, and CCCs for inter-site reproducibility. All intra-site ICCs showed high correlation, except for $T_{1\rho}$ at Site 4, where two subjects showed more than 10ms difference between scan and rescan for the patellar and trochlear cartilages. The relaxation times had low correlation

between sites. Relaxation times from Site 2 were higher than at other sites: 14.88ms (95%
CI [3.48, 26.27]) for $T_{1\rho}$ and 19.02ms (95% CI [8.16, 29.88]) for T_2.

The SNR efficiency for volunteers ranged across sites from 24 to 34 (Table 3c). The CVs
between the volunteer relaxation times fitted with 8 echoes and the two sets of 4 echoes
were less than 3%.

III.4 DISCUSSION

To successfully use cartilage of $T_{1\rho}$ and T_2 values in large-scale studies and clinical
trials, accuracy and stability of these measures across sites and equipment needs to be
ensured. In this study, we implemented 3D $T_{1\rho}$ and T_2 imaging based on the same sequence
structure (MAPSS) on MR platforms from three vendors (Siemens, GE, Philips), and
analyzed the repeatability and reproducibility of the relaxation measurements in a multi-
site, multi-vendor approach.

In our single-site phantom analysis, 3D MAPSS showed robust changes in
parameters, including with or without parallel imaging, time of recovery, and views-per-
segment. Compared with using the constant flip angle, MAPSS sequence design
(magnetization reset, RF cycling and variable flip angle train) helped mitigate the effect of
T_1 recovery and provided stability to views-per-segment.[13] The choice of preparation TEs
did not influence the T_2 measures, showing minimal variation (CV=1.02%), thus ensuring
that the different corrected TEs on different MR systems would have no significant effects
on T_2 measurement.

The acquisition time for 8-echo $T_{1\rho}$ or T_2 imaging for the whole knee with 8-echo
was longer than 10 minutes, which increased the risk of motion during the scan and thus

was not ideal for clinical implementation. Since our fitting results from 8 echoes and 4 echoes for $T_{1\rho}$ and T_2 in both phantoms and volunteers showed little differences (<1% in phantoms and <3% in volunteers), clinical applications using mono-exponential fitting of only 4 echoes may provide reliable measures with shorter imaging time. Using 4 echoes, the acquisition time would be reduced to 7 minutes. Furthermore, this may be combined with fast $T_{1\rho}$ and T_2 imaging based on novel techniques such as compressed sensing or deep-learning reconstruction that are being developed,[32-34] which will greatly facilitate clinical translation of $T_{1\rho}$ and T_2 imaging.

Our intra-site phantom and volunteer measurements showed good repeatability at all four sites with low intra-site CVs (CV<3.5% for phantoms and <5% for volunteers), with results comparable to previous single-site studies,[14, 15, 22] indicating successful implementation on all MR platforms.

Our inter-site CVs were higher than single-site repeatability as summarized by Mackay et al,[10] and higher than previous single-vendor multi-site studies reports (average CV of 4.9% for $T_{1\rho}$ and 4.4% for T_2[14] and 3.3-6.5% for T_2[21]). The factors to be addressed for reduction of inter-vendor inter-site variability can be categorized by their sources: hardware (MRI systems, RF coils), software (acquisition sequences and reconstruction and post-processing software), and environmental factors.

The most significant inter-site differences observed during this study were caused by different sequence structures. When we limited our analysis to sites using the same sequence structure (MAPSS), i.e, we excluded data from the one site using a different pulse sequence structure (Site 2), the overall inter-site CVs decreased from 14% to 8% and from 20% to 10% for $T_{1\rho}$ and T_2, respectively, confirming the dependency of relaxation times

on sequences reported in previous studies.[23-25] The difference between the two sequences was more pronounced for T_2 since the acquisitions had greater variation in the T_2 preparation scheme as compared to the $T_{1\rho}$, preparation, in addition to the different read-out structures. 3D MAPSS utilized a train of refocusing pulses with phase modulation (MLEV) for T_2 preparation and TE correction.[35] On the other hand, the segmented GRE acquisition used T_2 preparation with single refocusing pulse. Another factor for slightly lower CVs for $T_{1\rho}$ compared to T_2 could be less magic angle effect in $T_{1\rho}$ imaging, due to spin-lock pulses.[36, 37]

Another potential source of variability is inter-site scanner difference (including B_0 inhomogeneity profiles) due to different loading inside the scanner and different shimming algorithms employed by each vendor. The RF coils used in this study also had different structures, which will introduce different B_1 profiles. Although the MAPSS sequence is designed to be robust to B_0 and B_1 inhomogeneity with composite tip-down and tip-up pulses, phase shift in the middle of spin-lock pulses, and RF cycling,[13, 15, 38] residual artifacts could have caused higher inter-site variability, especially for volunteer imaging where inhomogeneity issues are greater.

In addition, different coils may result in different SNR, which can potentially introduce variations in relaxation time fitting, as consistent with previous reports,[14, 21] especially for the volunteer imaging with relatively low SNR of last echo images.

To prevent variations that can be introduced by different fitting algorithms, centralized processing was performed at a single site.[39, 40] However, the differences in DICOM image reconstruction between vendors (different filtering and regularization during reconstruction) should be noted. Although the retrieval, storage, and transmission

of raw data, including complex data, is challenging, these inter-vendor variations in image reconstruction indicate a potential need to collect the raw k-space data for centralized, uniform, single-algorithm image reconstruction across MR systems and sites in future studies.

Environmental factors, such as phantom temperature at the time of measurement, may explain some of the variability in our phantom measurement results, as the site with the lowest temperature had longer relaxation times. Potential differences in knee positioning of traveling volunteers at each site may have added to inter-site variation. Also, even though all images of traveling volunteers were visually checked for registration success, high inter-site CVs were observed for patellar and trochlear cartilage, the areas that are most challenging to register given differences in knee rotation. These regions are also highly susceptible to magic angle artefact due to their structural orientations.

The phantom measurements across sites were highly correlated, and with the high correlation of $T_{1\rho}$ and T_2 values between sites, a calibration model could be built for pool analysis between sites. However, large data sets for both phantoms and traveling volunteers need to be collected before a calibration model can be developed. Our current human cartilage relaxation times were uncorrelated, but this could be due to the limited number of volunteer data points and the smaller range of relaxation times compared with the phantom (since the data was collected with healthy volunteers only).

When measuring treatment effect during clinical trials, it is important to consider the measurement imprecision that is due to both between- and within-subject (i.e., test-retest measurement error) variability. Obuchowski et al.[41] determined how to estimate the necessary sample size for a clinical trial using a quantitative imaging biomarker with

known measurement error. For example, cross-sectional studies comparing controls and osteoarthritis patients report mean T_{1p} and T_2 values for 20 subjects.[20] Using this methodology, an intra-site measurement error of 4% would increase the sample size of such a clinical trial by 1-2 subjects, whereas an inter-site measurement error of 10% would increase the sample size by 9 subjects. For a longitudinal study of ACL-injured knees reporting one-year changes in injured and control knees of 40 patients and 15 controls,[29] factoring in these intra-site and inter-site measurement errors would increase the sample size by 5 and 12 subjects, respectively. Thus, the results from our study suggest that $T_{1\rho}$ and T_2 imaging with harmonized sequences and protocols and centralized post-processing are promising quantitative imaging biomarkers for future OA clinical trials.

Despite the promising results, there are several limitations to this study. The phantoms were not scanned before they were distributed to different sites. However, the four phantoms used in this study were manufactured from one batch. Furthermore, we analyzed T_{1p} and T_2 of three other identical phantoms that were manufactured from the same batch, but not used in this study at Site 1. The CVs of T_{1p} and T_2 values among these three phantoms and the one used in this study at Site 1 were approximately 1.2% and 1.44%, respectively, suggesting minimal inter-phantom variations. The pre-scan activities of traveling volunteers were not standardized and the scans were not performed at the same time of day, which may introduce diurnal variations.[15] However, all volunteers sat for 30 minutes before the scan to minimize potential effects from loading status differences. B_0 and B_1 corrections were not performed, which may have helped mitigate the inter-site variation. Lastly, the study was limited by the small sample size, and no patients with diagnosed cartilage degeneration were studied.

In conclusion, 3D $T_{1\rho}$ and T_2 imaging at 3T with the same sequence structure (MAPSS) has been developed on three major MR platforms, showing promising reproducibility with controlled sequence structure and parameters, and centralized post-processing methods. Additionally, our results indicate that the required scan times can be reduced when using four echoes, rather than eight, without loss of data reliability, making $T_{1\rho}$ and T_2 mapping more feasible and cost-effective for clinical practice. Larger-scale studies with controls and OA patients are warranted to further develop ways to mitigate inter-site and inter-vendor variation of cartilage relaxation time. Strategies for measurement calibration between sites and vendors are required in order to facilitate the application of the quantitative measures for multi-site multi-vendor clinical trials.

III.5 ACKNOWLEDGEMENTS

CHAPTER IV: ROBUST T1ρ PREPARATIONS: B1 AND B0 INHOMOGENEITY AND T2ρ EVALUATION WITH BLOCH EQUATION-BASED SIMULATION

IV.1 INTRODUCTION

For successful clinical translation of quantitative $T_{1\rho}$ imaging, the imaging technique still requires large amount of data to reliably characterize the disease in a clinical MRI. In this process, efficient data collection and evaluation will greatly facilitate the process, and this can be achieved by implementing the imaging method in multiple scanners and vendors, which was done in Chapter III. Although it showed promising results, the imaging method still has rooms for improvements in terms of robustness to system imperfections and scan-to-scan variations to successfully merge the data collected from different scanners.

One of the most significant system imperfections and scan-to-scan variations are B_0 and B_1 inhomogeneity, where both can be caused by scanner calibration, different coil design, and difference in loading (e.g. size and position of the volunteer). Such problem is more severe with 7T scanner. To overcome this challenge, many $T_{1\rho}$ preparation pulse designs have been investigated to mitigate the B_0 and B_1 inhomogeneity variation.[38, 42-48] Among different techniques, adiabatic $T_{1\rho}$ shows better robustness to inhomogeneities compared to continuous-wave $T_{1\rho}$ due to the characteristics of adiabatic pulse, but the technique is not feasible in 7T scanner due to specific absorption rate (SAR) limitation. Therefore, only continuous-wave $T_{1\rho}$ preparation schemes were evaluated and improved in this study.

When comparing different preparation schemes, it is very inefficient and time consuming to evaluate the different preparation pulses using physical acquisitions. This can be handled more efficiently with numerical simulation methods to investigate the preparation pulses in various B_0 and B_1 inhomogeneities.

In this study, six different preparation methods were evaluated. Bloch equation-based numerical simulation was implemented and verified with actual phantom acquisition. The simulation was used to efficiently evaluate the different preparation methods with varying B_0/B_1 inhomogeneity setup. In-vivo volunteers were scanned in both 3T and 7T scanner and the results were compared with observations from simulation results.

IV.2 METHODS

IV.2.1 B_0/B_1 Inhomogeneity Induced Error
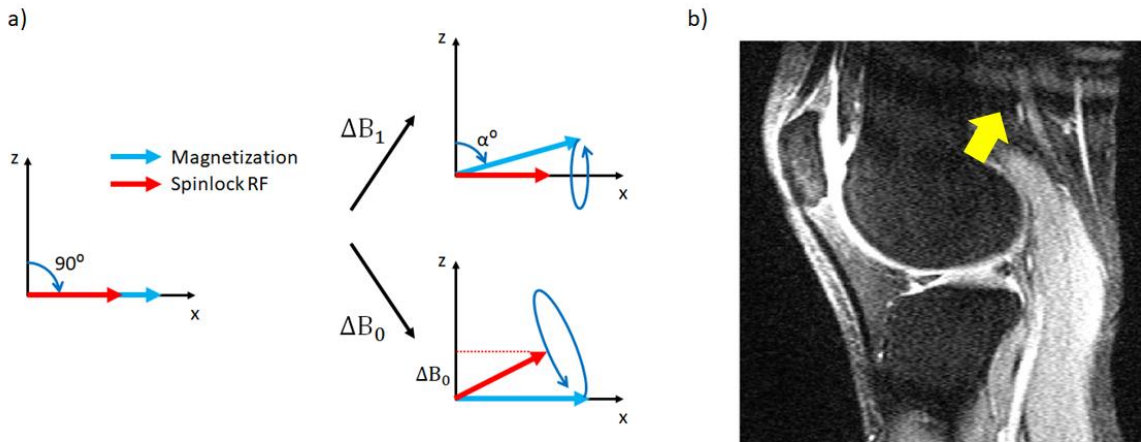
Figure 10 Effect of B_0 and B_1 inhomogeneity on spinlock $T_{1\rho}$ preparation. a) In an ideal situation, magnetization is locked in the transversal plane with spinlock RF pulse parallel to the magnetization. With the introduction of B_0 and B_1 inhomogeneity, magnetization is no longer parallel to the spinlock RF pulse, and the angle created between the two causes the magnetization to rotation. When B_0 inhomogeneity is present, applying two spinlock

As seen in Figure 10a, $T_{1\rho}$ involves spin-lock preparation, where, in an ideal situation, the magnetization is nutated to the transverse plane by a 90-degree pulse, followed by a spinlock RF pulse that is parallel to the nutated magnetization. In the presence of B_0 and B_1 inhomogeneity, an angle is created between the magnetization and spinlock RF pulse to create an angle in between, making the magnetization precess around the spinlock RF pulse. Such precession causes periodic fluctuation in the prepared magnetization, and even null the signal in extreme cases, resulting in banding-like artifact in the echo images (Figure 10b). When flip up and flip down RF pulses have finite length, B_0 inhomogeneity will precess the magnetization during this RF pulse, further increasing the angle between the magnetization and spinlock RF pulse. Furthermore, the magnetization doesn't simply relax with $T_{1\rho}$ relaxation, but also with $T_{2\rho}$ relaxation since the magnetization has component perpendicular to the spinlock RF pulse.

IV.2.2 $T_{1\rho}$ Preparation Schemes
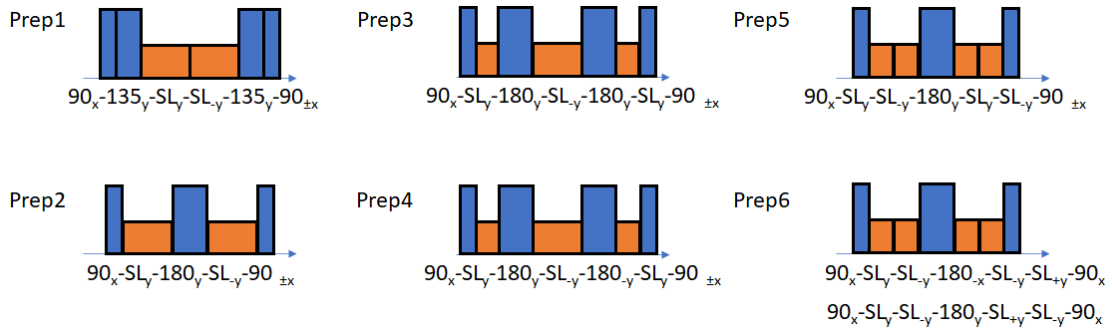
Figure 11 $T_{1\rho}$ preparation pulses evaluated in the study (Prep1,[42] Prep2,[43] Prep3,[44] Prep4,[45] Prep5,[46] Prep6: modified from Prep 5) In the preparation pulses, 180-degree pulses were used as refocusing pulses in spin-echo T_2, and spinlock RF pulses were partitioned with 180-degree phase difference to achieve the similar effect as refocusing.

For the data acquisition, 3D MAPSS sequence was used with mono-exponential fitting to create $T_{1\rho}$ and $T_{2\rho}$ maps. Six $T_{1\rho}$ preparation schemes that include flip-up and flip-down preparations for phase cycling in MAPSS sequence were implemented and evaluated in both simulation and on scanner, shown in Figure 11. The phase of the last 90-degree RF pulse was flipped by 180 degrees accordingly to accommodate the flip-up and flip-down preparation. The schemes 1-5 (Prep1 - Prep5) were proposed in the literature,[42-46] and we proposed the scheme 6 (Prep6) in this study. For Prep6, phase of the Prep5 was manipulated in a way that will compensate for the B_1 inhomogeneity better in both flip up and flip down preparation.

IV.2.3 Bloch Equation-Based Simulation
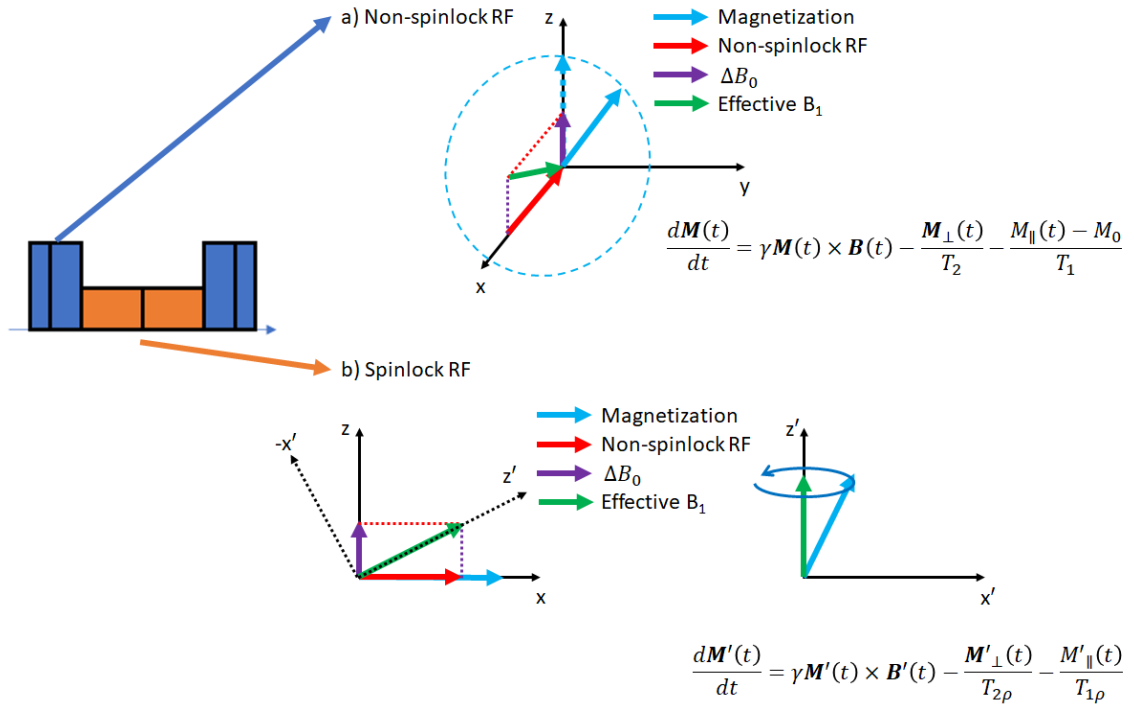
Figure 12 Schematic of the non-spinlock and spinlock RF pulses and corresponding signal equation.

To efficiently simulate the B_0 and B_1 inhomogeneity caused error in spinlock RF pulse, spinlock preparation was simulated based on Bloch equation using MATLAB. Relaxation properties such as T_1, T_2, $T_{1\rho}$, and $T_{2\rho}$ and pulse width equivalent to the scanner implementation (400 µs for 90-degree pulse) were accommodated. Time intervals of 1 µs was used to approximate the continuous-time magnetization change. The preparation RF pulses were classified into two parts, non-spinlock RF pulses such as tip-down and tip-up 90-degree pulse and 180-degree refocusing pulse (Blue pulses in Figure 11), and spinlock RF pulses which will cause $T_{1\rho}$ and $T_{2\rho}$ relaxation (Orange pulses in Figure 11). For non-spinlock RF pulses, signal evolution follows the typical Bloch equation with T_1 recovery and T_2 decay, Figure 12a. For spinlock RF pulses, the coordinate system was rotated so

that the z'-axis of the rotated coordinate system aligns with the effective B_1 direction, which is the sum of the B_0 inhomogeneity and the applied spinlock RF pulse, Figure 12b. In this coordinate system, z'-magnetization decays with $T_{1\rho}$ time constant without recovery, and xy'-magnetization decays with $T_{2\rho}$ time constant. In this rotated coordinate system, the longitudinal magnetization and transverse magnetization does not change their position relative to the z'-axis since effective B_1 field in the rotated frame also stays in the z'-axis. This can simplify the solution of the equation to,

$$\boldsymbol{M'}_{\perp}(t + TSL) = \exp\left(-\frac{TSL}{T_{2\rho}}\right) R\big(TSL \times \gamma B_{1,eff}\big)\boldsymbol{M'}_{\perp}(t)$$

$$\boldsymbol{M'}_{\parallel}(t + TSL) = \exp\left(-\frac{TSL}{T_{1\rho}}\right) \boldsymbol{M'}_{\parallel}(t)$$

Where *TSL* is the length of the spinlock RF pulse, $R\big(TSL \times \gamma B_{1,eff}\big)$ is the rotation matrix in xy' plane by angle $TSL \times \gamma B_{1,eff}$. This greatly shortens the simulation time since now there is no need to approximate the continuous-time motion with small time interval for lengthy spinlock pulses (e.g. simulating 40 ms spinlock pulse with 1 µs interval).

IV.2.4 Phantom Scan

The simulation was first validated by phantom scan. A 4 % (weight/weight) agarose phantom was created in distilled water. 3D MAPSS was scanned with 6 different $T_{1\rho}$ preparations and a $T_{2\rho}$ preparation using a 3T MR scanner (Magnetom Prisma, Siemens Healthcare AG, Erlangen, Germany) with a 1Tx/20Rx head coil. The following scan parameters were used; FOV=140x140 mm^2, slice thickness = 5 mm, imaging matrix = 256x128x8, T1 recovery time = 1.5 s, spinlock frequency (SLF) = 500 Hz, time of spinlock (TSL) = 0, 10, 20, 30 ms. First, the phantom was carefully shimmed to acquire all

acquisitions on-resonance, and the phantom was scanned again with a 300µT/m gradient field using shim coil to apply ±250 Hz inhomogeneity in 4cm range. The B0 was measured by double-echo gradient-echo sequence, and B_1 was measured by Bloch-Siegert shift B_1 mapping. The simulation result was generated using the on-resonance $T_{1\rho}$ and $T_{2\rho}$ values and measured B_0 and B_1 maps in off-resonance situation and compared to the measured off-resonance $T_{1\rho}$ value.

After verification, the B_0 and B_1 combinations were further expanded and evaluated with the simulation. T_1, T_2, and $T_{1\rho}$ were set to 1200 ms, 40 ms, and 40 ms, respectively. $T_{2\rho}$ was varied from 40 to 70 ms with 5 ms interval to investigate the influence of $T_{2\rho}$ on the $T_{1\rho}$ quantification error. B_0 was varied from -200 to 200 Hz, and nominal B_1 was varied from 0.8 to 1.2. For comparing the performance of the preparation pulse, proportion of area under 5% quantification error with respect to the simulated B_0 and B_1 range was calculated.

IV.2.5 Volunteer Scan

For volunteer scan, knee from 3 volunteers were scanned at 3T MR scanner using 1Tx/15Rx knee coil (QED, Mayfield, OH), and one volunteer was scanned at 7T MR scanner (Magnetom Terra, Siemens Healthcare AG, Erlangen, Germany) using 1Tx/28Rx knee coil (QED, Mayfield, OH). All procedures were approved by the Institutional Review Board (IRB). 3D MAPSS was scanned with 6 different $T_{1\rho}$ preparations and a $T_{2\rho}$ preparation. The following scan parameters were used for 3D MAPSS; FOV=140x140 mm^2, slice thickness = 4 mm, imaging matrix = 320x160x24, T1 recovery time = 1.5 s, spinlock frequency (SLF) = 500 Hz, time of spinlock (TSL) = 0, 10, 30, 70 ms (3T), 0, 10, 20, 40 ms (7T).

Additionally, dual-echo steady-state (DESS) sequence was scanned for automatic cartilage segmentation using deep learning.[49] Six cartilage compartments were segmented, which included the medial/lateral femoral condyle (MFC/LFC), medial/lateral tibial (MT/LT), trochlear (TRO), and patellar (PAT) cartilage.

Coefficient of variations (CV) was calculated to evaluate the $T_{1\rho}$ quantification differences between the six $T_{1\rho}$ preparations. $T_{1\rho}$ and $T_{2\rho}$ values were compared to identify the range of $T_{1\rho}$ and $T_{2\rho}$ in-vivo and identify which relaxation parameters should be used to evaluate the preparation performance. For 7T acquisition, the oscillation caused by severe B_0 and B_1 inhomogeneity was quantitatively compared between different preparation schemes by calculating the root-mean-squared error (RMSE) to the fitted mono-exponential decay curve. The following equation was used for calculation.

$$RMSE = \sqrt{\frac{\sum_{i=1}^{n}\left(S(TSL_i) - S_0 \exp\left(-\frac{TSL_i}{T_{1\rho\_fit}}\right)\right)}{n}}$$

Where n is number of echoes, $S(TSL_i)$ is the acquired signal at TSL_i, and S_0, $T_{1\rho\_fit}$ are fitted value from mono-exponential decay fitting. Low RMSE will imply the amount of oscillation caused by B_0 and B_1 inhomogeneity was small, thus the preparation is robust to B_0 and B_1 inhomogeneity. This evaluation was not performed in 3T acquisition since the amount of B_0 and B_1 inhomogeneity was not severe enough to show the difference.

IV.3 RESULTS

IV.3.1 Bloch Simulation Results and Phantom Results
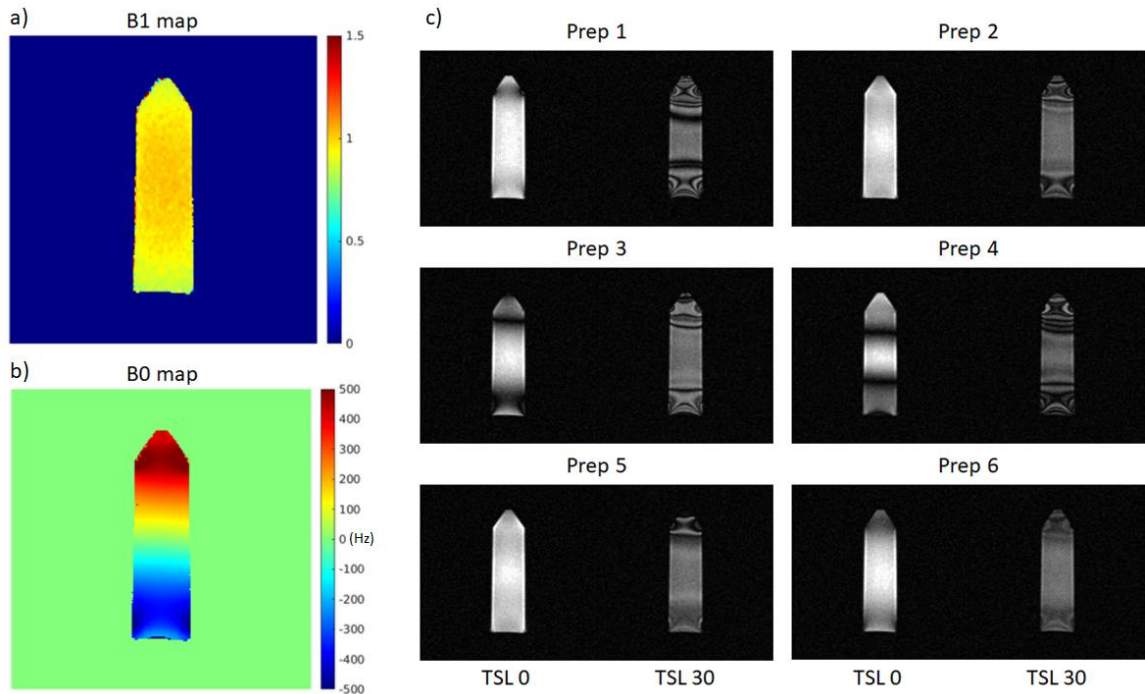
Figure 13 Phantom acquisition results. a) shows the B_1 inhomogeneity map and b) shows the B_0 inhomogeneity map. c) shows the $T_{1\rho}$-weighted echoes at TSL 0 and 30 ms. The echo images clearly show the banding-like artifact created by the added B_0 inhomogeneity.

Figure 13 shows the phantom acquisition result with added B_0 inhomogeneity. The B_0 inhomogeneity map (Figure 13b) shows the added gradient field using shim coil successfully created a range of inhomogeneity that can used to validate the simulation result in a wide range of B_0 and B_1 combinations.
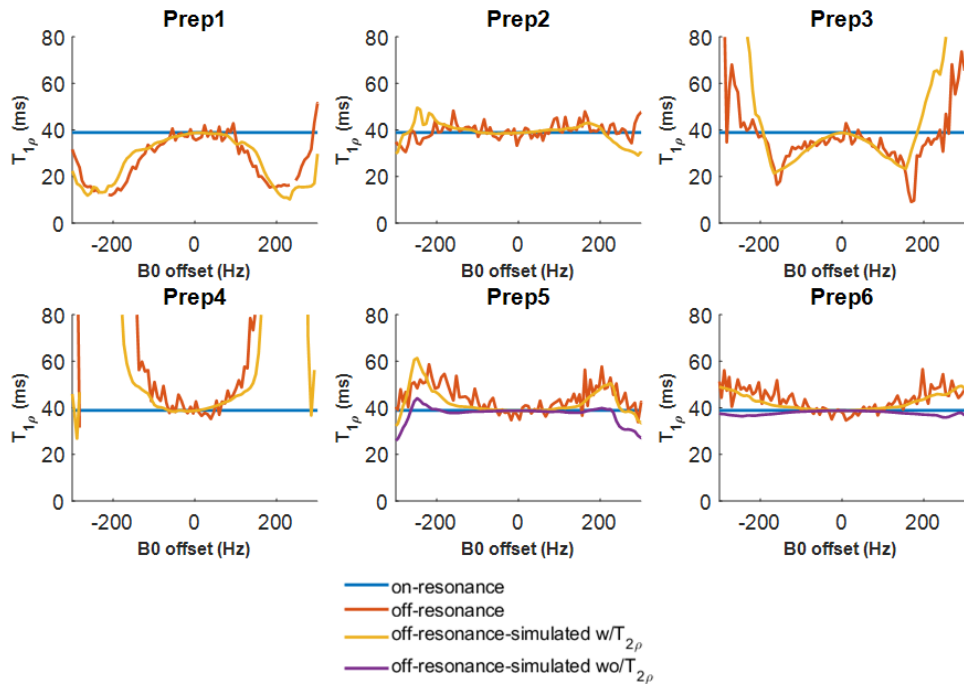
Figure 14 The comparison between phantom acquisition data (red line), simulation prediction with $T_{2\rho}$ (yellow line), and simulation prediction with $T_{2\rho}$ (purple line). The $T_{1\rho}$ value deviate away from the on-resonance reference value (blue line) with added B_0 inhomogeneity, and simulation was able to predict and follow the pattern of deviation.

The on-resonance reference value of phantom relaxometry were as follows; $T_1 =$ 2200 ms, $T_2 = 40$ ms, $T_{1\rho} = 40$ ms, $T_{2\rho} = 68$ ms. The prediction of $T_{1\rho}$ values using these phantom relaxometry parameters and the B_0 and B_1 inhomogeneity maps (Figure 13a, b) by the Bloch simulator is shown in Figure 14, along with the $T_{1\rho}$ values calculated from the actual acquired data. The simulation reflects the actual acquisition, verifying that the simulation can be used to evaluate different preparations. Note that the addition of $T_{2\rho}$ was crucial especially for Prep5 and 6, where the purple line in Figure 14 was not able to predict the overestimation with B_0 and B_1 inhomogeneity when $T_{2\rho}$ was set the same as $T_{1\rho}$.
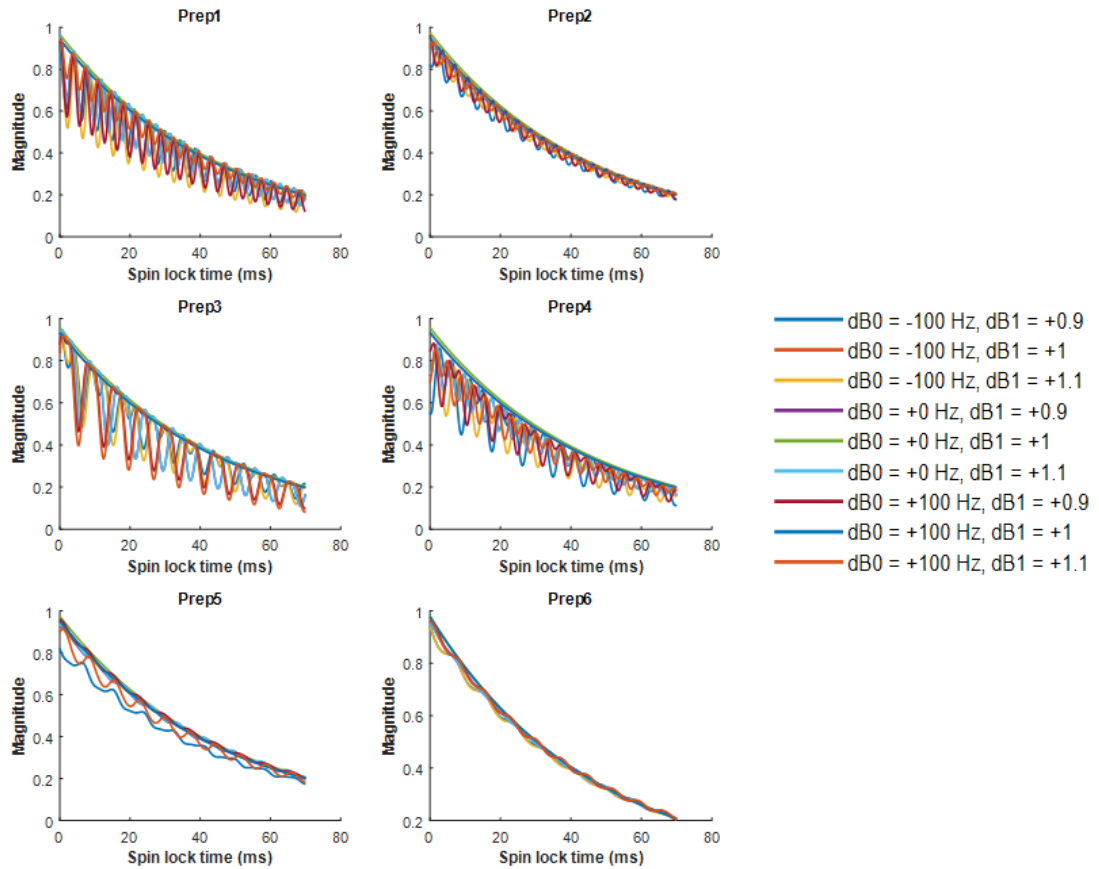
Figure 15 $T_{1\rho}$ decay curves in different preparations under B_0 and B_1 inhomogeneity. All curves showed the expected oscillating patterns. Prep6 showed least amount of oscillation, both in amplitude and frequency.

Figure 15 shows the example $T_{1\rho}$ decay curve using $T_{1\rho}$ and $T_{2\rho}$ of 40/70 ms in different B_0 and B_1 inhomogeneity combinations. All curves show the expected oscillation pattern with the added off-resonance. Among the curves, Prep6 showed the least amount of oscillation. This can also be verified with the phantom acquisition, Figure 13c, where Prep6 shows least amount of banding artifact even with severe B_0 and B_1 inhomogeneity.
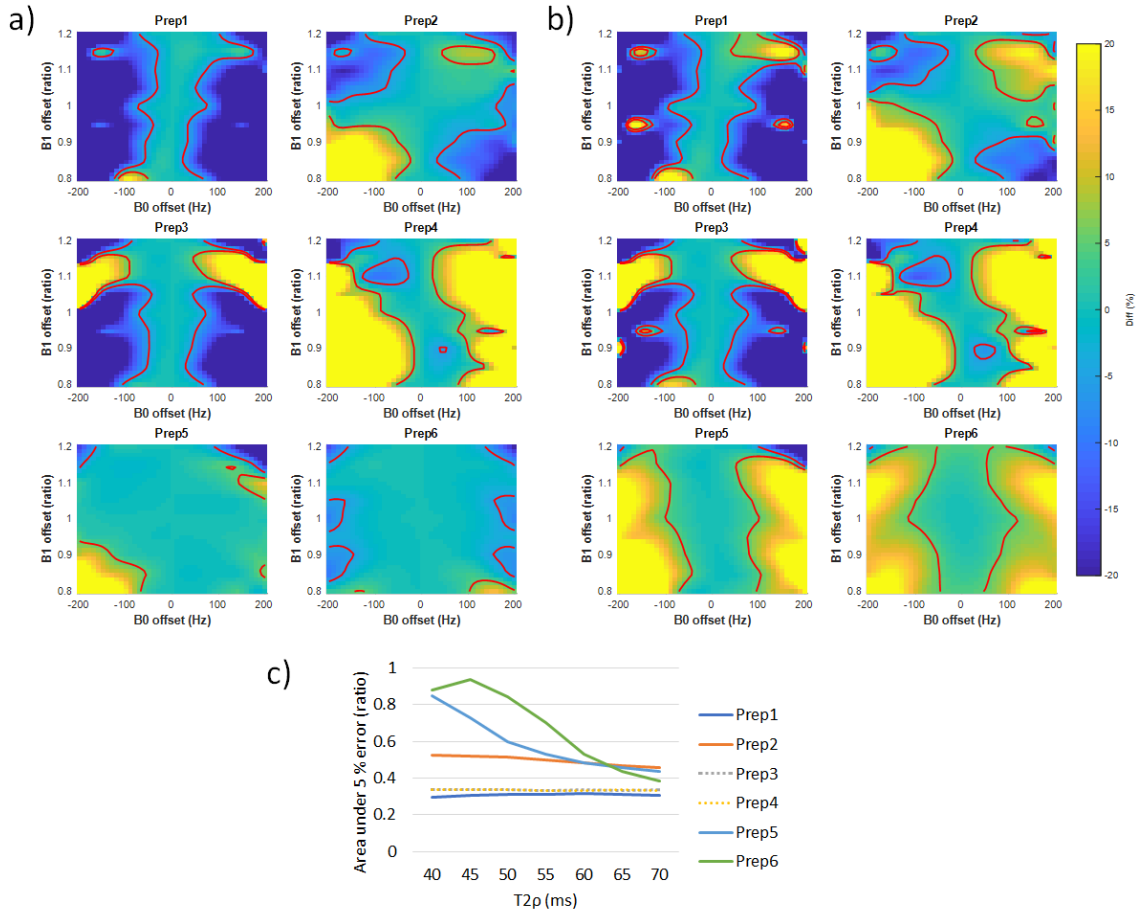
Figure 16 Heatmap of $T_{1\rho}$ quantification error with different B_0 and B_1 inhomogeneities with a) $T_{2\rho}$ = 40 ms and b) $T_{2\rho}$ = 70 ms. Red contour line shows the ±5 % T1rho quantification error. Note that the heatmap changes with different $T_{2\rho}$, and such $T_{2\rho}$ contamination is more pronounced for Prep5 and 6. c) area under 5% error plot with respect to T2rho. The $T_{1\rho}$ reference value was 40 ms for all simulation cases.

Figure 16 shows the heatmap of $T_{1\rho}$ quantification error with different B_0 nad B_1 inhomogeneities. Larger area under 5% error (red contour lines) indicates the preparations is more robust to B_0 and B_1 inhomogeneity. Figure 16a indicates that, with $T_{1\rho}$ = 40ms, and $T_{2\rho}$ = 40ms, Prep 5 and 6 showed the largest area under 5% error; while Figure 16b indicates that, with $T_{1\rho}$ = 40ms, and $T_{2\rho}$ = 70ms, Prep2 showed largest area under 5% error,

slightly larger than Prep5 and Prep6. Figure 16c indicated that the gap between $T_{2\rho}$ and $T_{1\rho}$ value had the most influence for Prep5 and 6, with the and area under 5% error increasing as the gap between $T_{2\rho}$ and $T_{1\rho}$ decreased. Prep6 showed the largest area under 5% error when the gap was smaller than 25 ms. In contrast, Prep2 was less affected by the difference between $T_{1\rho}$ and $T_{2\rho}$ values.

	T2ρ	Prep1	Prep2	Prep3	Prep4	Prep5	Prep6	CV (%)
MFC	52.2	45.9	46.0	45.8	45.9	45.4	45.5	1.4
MT	47.2	43.7	42.7	43.6	42.9	42.9	42.0	2.5
LFC	49.9	42.1	42.5	42.7	42.1	41.9	41.6	2.2
LT	45.1	39.5	38.8	40.4	40.3	39.8	39.1	2.1
TRO	56.0	47.9	47.3	47.8	47.6	46.4	46.1	1.8
PAT	51.0	41.3	44.2	42.3	43.6	41.4	41.2	3.1
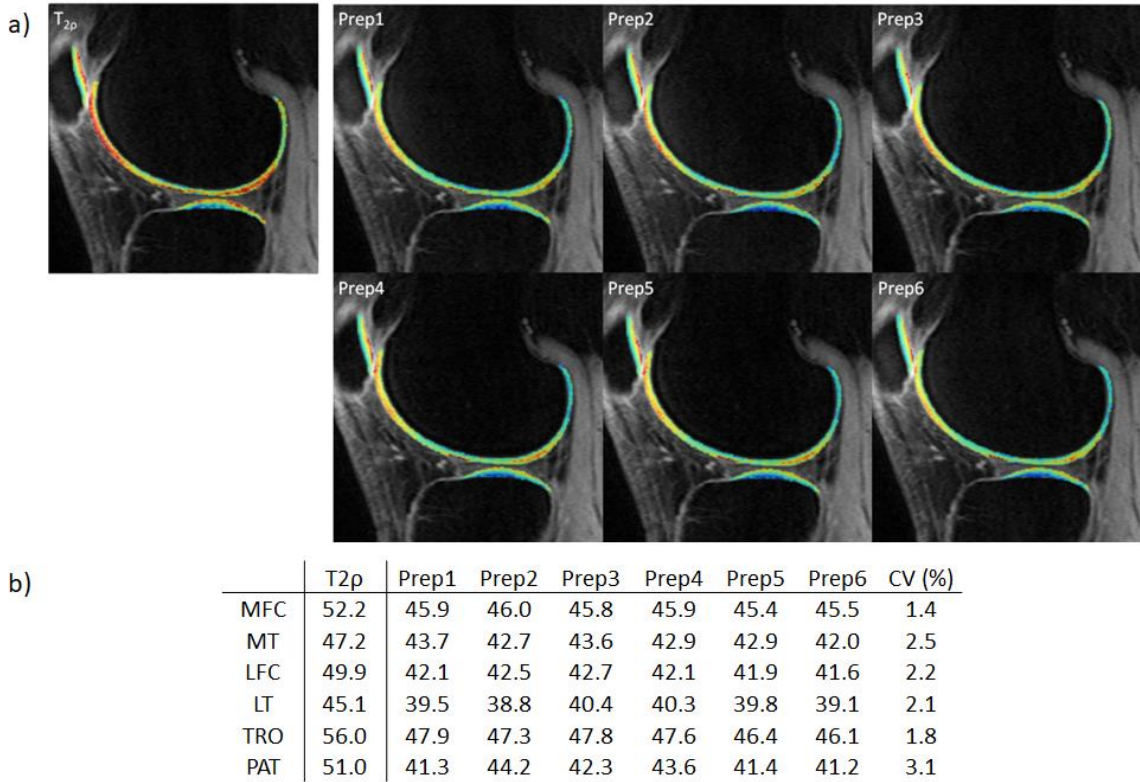
Figure 17 a) Example $T_{2\rho}$ and $T_{1\rho}$ maps with different preparation pulses and b) compartment $T_{1\rho}$ and $T_{2\rho}$ mean values from the three volunteers using the 3T MRI scanner.

Figure 17 shows quantification results of human subjects from 3T scanner. As shown in the map and compartment mean values, the $T_{1\rho}$ values did not vary between different preparation schemes (2.2±0.6% average CV) due to small B_0 and B_1 inhomogeneity at 3T. Differences between compartment $T_{1\rho}$ and $T_{2\rho}$ values were ranging from 4.2 to 8.8 ms (6.9±1.8 ms overall).

Figure 18 a) Example $T_{1\rho}$ maps with different preparation pulses and b) compartment $T_{1\rho}$ mean values using thein 7T MRI scanner. The $T_{2\rho}$ result was omitted due to significant B_0 and B_1 inhomogeneity induced error.

Figure 18 shows the quantification result from 7T scanner. Due to significant B_0 and B_1 inhomogeneity, $T_{2\rho}$ preparation could not provide feasible value. Also, $T_{1\rho}$ values provided by different preparation schemes showed larger variation compared to 3T (average CV 2.2±0.6% in 3T and 4.5±2.1% in 7T).
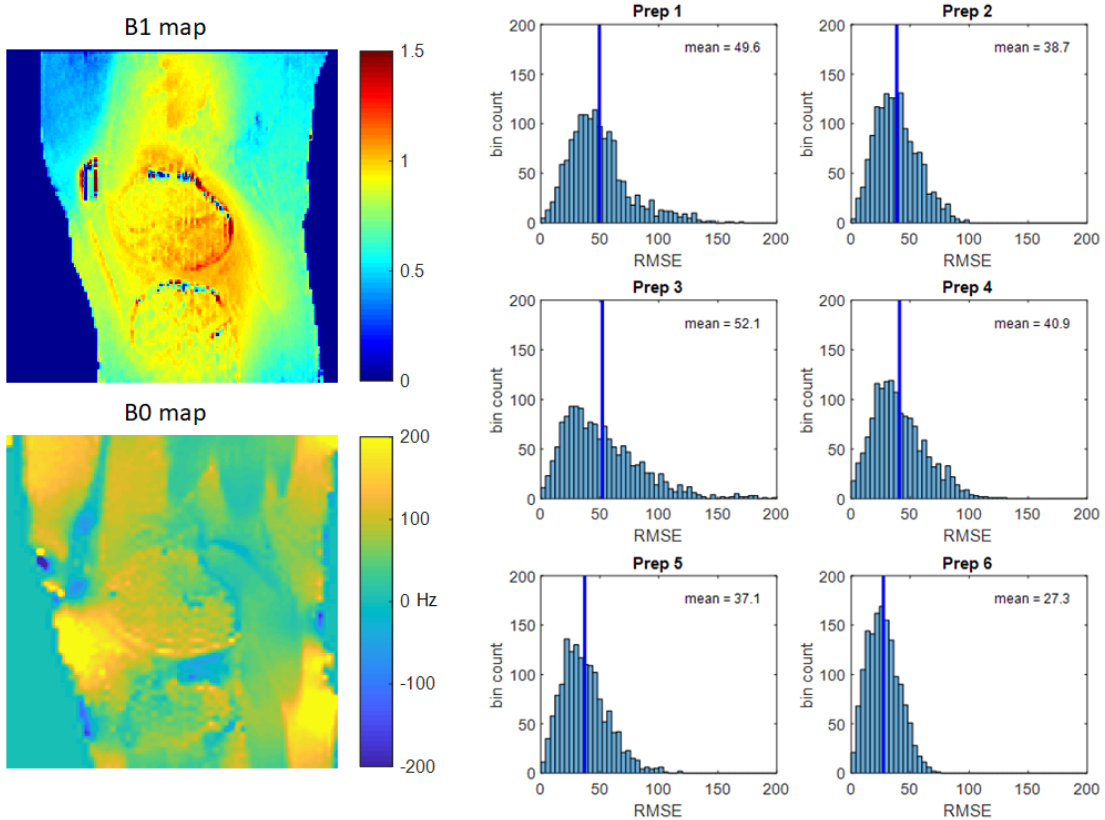
Figure 19 Example B_0 and B_1 inhomogeneity maps and corresponding histogram of mono-exponential fitting RMSE in cartilage. The B_0 and B_1 inhomogeneity had a similar range of values in cartilage as in the simulation (0.8 to 1.2 nominal B1, ±200 Hz B0 inhomogeneity).

Figure 19 shows the influence of the B_0 and B_1 inhomogeneity in the $T_{1\rho}$ preparation. The example slice showed significant B_0 and B_1 inhomogeneity in the cartilage, and the amount of oscillation inferred by the RMSE showed similar trend explained by the area under 5% error (Figure 16c), with Prep6 showing the smallest oscillation among the preparations.

IV.4 DISCUSSION

In this study, the robustness to B_0 and B_1 inhomogeneity of different $T_{1\rho}$ preparation schemes were compared using simulation, as well as phantom and volunteer scans. The simulation was able to explain the influence of the B_0 and B_1 inhomogeneities during the $T_{1\rho}$ preparation. The validation of the simulation with the phantom acquisition (Figure 14) showed that introduction of $T_{2\rho}$ contamination helped better predict the preparation results, especially for Prep5 and 6. The oscillation pattern in Figure 15 showed Prep6 had the smallest amplitude and frequency of oscillation among all preparations. Such reduced oscillation helps the $T_{1\rho}$ preparation to be more robust to B_0 and B_1 inhomogeneities. Another advantage of Prep6 from the oscillation pattern was that the signal loss was smaller than other preparations, which will result in better signal-to-noise ratio (SNR). Such advantages will be more pronounced with quantification of short $T_{1\rho}$ components.

The $T_{1\rho}$ quantification error heatmap in Figure 16 showed similar observations as from the oscillation patterns. Among the preparations, Prep5 and 6 were significantly influenced by $T_{2\rho}$ contamination, and the area under 5% error changed according to the gap between $T_{2\rho}$ and $T_{1\rho}$ value. For Prep6, the error caused by $T_{2\rho}$ contamination was greater than the robustness to the B_0 and B_1 inhomogeneity by smaller oscillation when the $T_{2\rho}$ was 25 ms longer than the $T_{1\rho}$ value. If $T_{2\rho}$ is less than 10 ms longer than $T_{1\rho}$, 80% of the B_0 and B_1 inhomogeneity combination within 0.8 to 1.2 nominal B1 and -200 to 200 Hz B_0 inhomogeneity had less than 5% quantification error, which can provide sufficient coverage in the in-vivo scan situations.

The volunteer scans at 3T and 7T provided evidence for the previous observations through simulation. As shown from heatmap in Figure 16, all $T_{1\rho}$ preparations showed good

quantification accuracy (under 5% error) within ±100 Hz B0 inhomogeneity. Quantification results from 3T volunteer scan showed average CV of 2.2 % between different preparation schemes, which is similar to the $T_{1\rho}$ quantification repeatability reported by a previous study (1.60-3.93%),[50] agreeing with the observation from the simulation. The difference between $T_{1\rho}$ and $T_{2\rho}$ was ranging from 4.2 to 8.8 ms, and in this scenario, Prep6 yielded the best quantification accuracy in the simulation (Figure 16c).

7T volunteer scan showed bigger B_0 and B_1 inhomogeneities compared to 3T scans, with B_0 inhomogeneity ranging to ±200 Hz in the cartilage region (Figure 19). This resulted in bigger difference between different preparation schemes with average CV 4.5±2.1%. The amount of oscillation inferred by the RMSE from mono-exponential fitting also agreed with the simulation result. Prep6 showed lowest mean RMSE, which implies smallest oscillation and complies with the simulation result from Figure 15. Assuming the difference between $T_{1\rho}$ and $T_{2\rho}$ is similar in 7T compared to 3T, the quantification error is influenced more by the oscillation rather than the $T_{2\rho}$ contamination, and the trend of mean RMSE corresponds well to the trend of area under 5% error in Figure 16c except for Prep4. To sum up all previous observations, Prep6 provides the most robust $T_{1\rho}$ preparation in the human knee scans.

Several aspects require further investigation. First, the simulation was not evaluated in samples with $T_{1\rho}$ and $T_{2\rho}$ dispersion. The agarose phantom used for validating the simulation did not have $T_{1\rho}$ dispersion (no difference between T_2 and $T_{1\rho}$). Human tissues typically have $T_{1\rho}$ dispersion characteristics, where $T_{1\rho}$ values change with different SLFs.[51] Such factor could change the final evaluation of $T_{1\rho}$ preparations in a way where $T_{2\rho}$ and $T_{1\rho}$ difference becomes larger or smaller depending on the size of the effective

spinlock RF pulse. Moreover, the current model could be insufficient to explain the $T_{1\rho}$ dispersion phenomenon since it is strictly based on classical mechanical interpretation of MR physics.

Second, there are rooms of improvement by expanding the simulation to multi-exponential $T_{1\rho}$ evaluation. As explained briefly in the previous discussion, the influence of oscillation varies with the $T_{1\rho}$ value, and when there is mixture of different $T_{1\rho}$ components, the influence of oscillation can be different from the mono-exponential situation. Since there are infinite possible combinations of $T_{1\rho}$ components, the investigation will require narrowing down the target values based on in-vivo or specimen experiments for efficient evaluation.

Lastly, the oscillation pattern could lead to optimal choice of TSLs. The oscillation pattern, especially the frequency of the oscillation, relies on the size of the effective spinlock RF pulse causing the spinning of the magnetization. Therefore, there is possibility that optimal TSLs can be determined using the points with the least amount of oscillation with the target SLF and B_0 and B_1 inhomogeneities.

In conclusion, Bloch equation-based simulation was implemented and validated for evaluating $T_{1\rho}$ preparation. The simulation showed good accuracy by considering relaxation times including $T_{2\rho}$. With the simulation, different $T_{1\rho}$ preparations could be efficiently compared in different B_0 and B_1 inhomogeneities. Among the preparations, simulation results showed Prep6 was the most robustness to the B_0 and B_1 inhomogeneity with least amount of oscillation, and the volunteer scan results from 3T and 7T MRI scanners supported the simulation result. The simulation will be further developed by introducing realistic factors such as $T_{1\rho}$ and $T_{2\rho}$ dispersion and multi-exponential $T_{1\rho}$.

CHAPTER V: DEVELOPMENT OF A MUSCULOSKELETAL RELAXOMETRY PHANTOM FOR T1, T2, AND T1ρ MEASUREMENTS

V.1 INTRODUCTION

In the application of qMRI, it is important to account for and mitigate the inherent variability of qMRI methods stemming from the technical differences such as hardware, pulse sequence, imaging parameters, etc., since such technical variability can reduce the sensitivity of the qMRI method or even mask out important image features originating from pathological sources.[52] The use of physical phantom can greatly facilitate identifying the variability and help qMRI research in many aspects. For instance, there are various methods used to acquire relaxation times such as T_1, T_2, and $T_{1\rho}$, and including measurements using reliable and reproducible phantom will help comparing and consolidating results from different studies. Additionally, phantom experiments will enable standardizing and optimizing sequence parameters in large-scale multi-site multi-vendor studies and tracking scan quality in a longitudinal study. The high significance of phantom in qMRI led to development of such phantoms, and phantoms such as ACR phantom[53] and ISMRM/NIST MRI system phantom[54] were developed and became commercially available. These phantoms assisted numerous qMRI research. However, there are no commercially available phantoms that is dedicated to MSK research.

Therefore, the goal of the study was to develop a dedicated MSK relaxometry phantom that can be used for quality assurance of articular cartilage T_1, T_2, and $T_{1\rho}$ measures, with a focus on the knee joint.

V.2 METHODS

V.2.1 MSK Relaxometry Phantom Design Considerations

To create a phantom that will aid the relaxometry qMRI research in MSK, the following aspects were considered during the design. First, the materials in the phantom need to have relaxation properties that mimic the tissue characteristics of articular cartilage, which will greatly help predict the quantification error of the measurement method in an actual in-vivo tissue. Second, the phantom should be compatible with the commonly used knee RF coils. Since change of RF coil could also influence the qMRI result, it is important to ensure the phantom can fit in the RF coil used in the actual in-vivo scan. And lastly, the ability to measure temperature for possible temperature dependency of phantom material is required. Relaxation times are closely related with the temperature since the thermal movement of the material is one of the main factors of the MR phenomenon.

(a)
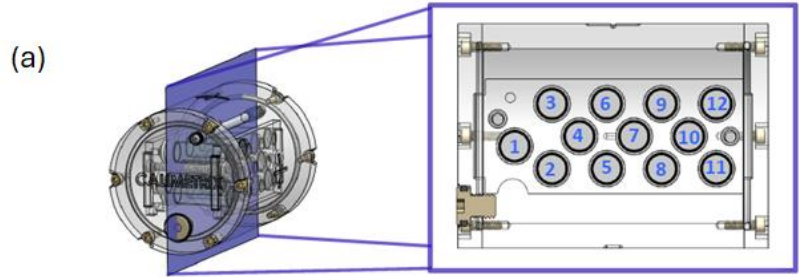
Location	1	2	3	4	5	6
Nominal T1/T2 [ms]	1200/10	1200/20	1200/30	1200/40	1200/50	1200/60
Location	7	8	9	10	11	12
Nominal T1/T2 [ms]	1200/70	1200/80	1200/90	1200/100	300/40	700/40

(b)

Figure 20 a) Vial position and nominal T_1 and T_2 for each vial. b) Picture of phantom placement on the coil with phantom stand. Phantom stand ensures the phantom is in the middle of the coil consistently.

With these aspects in mind, we developed a novel MSK Relaxometry Phantom in collaboration with NIST and Calimetrix (Madison, WI). The phantom is composed of a cylindrical phantom housing containing 12 vials filled with gels that simultaneously modulate T_1 and T_2. The target T_1/T_2 values of each vial when measured at 3T are: 1200/10, 1200/20, 1200/30, 1200/40, 1200/50, 1200/60, 1200/70, 1200/80, 1200/90, 1200/100, 700/40, 300/40 ms (Figure 20a). Each vial has a diameter of approximately 16 mm and length of 57 mm. The long axis of the vials is oriented perpendicular to the axis of the cylindrical housing, and the vials are positioned asymmetrically to avoid vial identification ambiguities. The housing is designed to fit inside commonly used knee coils and has a 4.5-

inch diameter and 6.25-inch length. The housing is filled with a doped water solution to optimize image quality and homogeneity. A NIST-traceable analog MR-visible incubator thermometer is embedded within the phantom to allow for precise temperature monitoring from both visual observation of the thermometer through the phantom wall and by analysis of phantom MR images. Finally, four custom external positioners ("stands") that interface with the curvature of commonly used MRI knee coils are provided to ensure repeatable phantom positioning with the housing parallel to the patient table. The specific RF coils for the phantom stands are QED 1Tx/28Rx, 15Rx knee coils, Philips 1Tx/8Rx, 16Rx knee coils, or equivalent.

V.2.2 MR Visible Thermometer
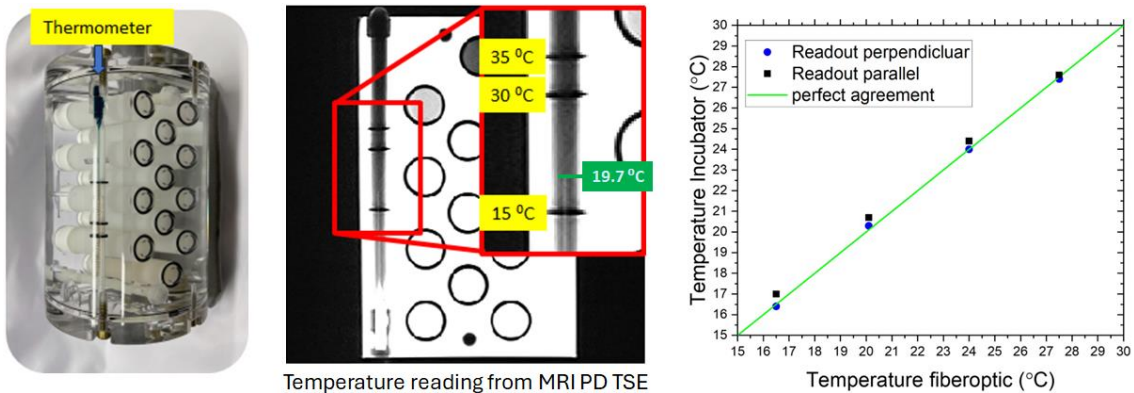
Figure 21 Temperature reading using MRI images. The thermometer placed inside the phantom measures the temperature of the liquid filling the phantom. The temperature is measurable using the MRI sequence (PD TSE) with the assist of two rubber rings located at 15, 30, and 35 °C. The MRI thermometer reading was verified with the fiberoptic thermometer reading and showed good agreement.

Figure 21 shows the incubator thermometer embedded in the phantom and the MR image of the thermometer. The thermometer fill was Enviro-Safe® Green Liquid, which is a citrus oil formulation with a green dye, and the fill was visible in PD TSE images without fat suppression. Since the material of the fill is oil, the chemical shift could lead to reading error if the frequency encoding direction of the image is along the thermometer axis. The relative position of the fill between the three rings located at 15, 30, and 35 ºC can determine the reading of the thermometer.

V.2.3 MRI T_1, T_2, and $T_{1\rho}$ Measurement

Key criterions for evaluating the performance of a phantom includes longitudinal stability, repeatability of the manufacture, and the multi-site multi-vendor measurement reproducibility. For these evaluations, MRI measurements were performed using two 3T MR scanners (Siemens Prisma with QED 1Tx/15Rx knee coil and GE Healthcare SIGNA Premier with AIR Anterior array coil). T_1 was measured using 2D inversion-recovery spin-echo (IRSE) sequence. T_2 was measured using single spin-echo (SE) and MLEV-16 (phase modulated CPMG)[35] prepared MAPSS sequence. $T_{1\rho}$ was measured using MAPSS sequence. Detailed sequence parameters are listed in Table 4. For IRSE T_1 and SE T_2, single-slice acquisition was used to avoid possible slice crosstalk and magnetization transfer from affecting the measurement. Overall protocol time of the Siemens IRSE T_1, SE T_2, MAPSS $T_{1\rho}$, and MAPSS T_2 was 30 minutes including the vendor-provided B_0 and B_1 mapping.

	TR (ms)	TE (ms)	FOV (mm2)	Matrix	Slice Thickness (mm)	Inversion Time (ms)
IR T1 (GE)	7000	Min	140x140	140x140x1	5	50, 400, 900, 1800
IR T1 (Siemens)	5500	7.1	140x140	256x128x1	4	23, 250, 400, 800, 1500, 2500
SE T2 (GE)	1000	11,16,21,28, 36,46,60	140x140	140x140x3	3	
SE T2 (Siemens)	1000	7.1, 10, 15, 30, 50, 70	140x140	256x128x1	4	
MAPSS T2 (Siemens)	Min	Min	140x140	256x128x20	5	
MAPSS T1rho (Siemens)	Min	Min	140x140	256x128x20	5	
Other parameters for MAPSS	Spin-lock frequency = 500 Hz, number of echoe = 4, T1 recovery time = 1500 ms Views per segment = 96, time of spinlock (T1rho) = [0, 10, 30, 70] ms TE (T2) = [0, 20, 40, 60] ms, with gap between refocusing pulse = 5.8 ms					

Table 4 Table of MRI acquisition parameters. Note that $T_{1\rho}$ was measured only at Siemens scanner due to availability of the imaging sequence.

A prototype phantom created from the first batch was scanned using the Siemens scanner. Multiple measurements over 9-months period were used to calculate longitudinal CV to evaluate the longitudinal stability of the phantom. In the second batch, 12 phantoms were created, where all phantoms were scanned using the Siemens and GE scanners to calculate the CV for intra-batch variability. CV between the average relaxation time of each batch was calculated to evaluate the inter-batch variability. These intra- and inter-batch can be used to assess the repeatability of the manufacture process. Finally, T_1 and T_2 measurements from the two different MR vendors were compared using Bland-Altman plot and CV.

V.2.4 NMR T_1, T_2, and $T_{1\rho}$ Measurement

Measurements using NMR spectroscopy is close to gold-standard due to its ability to control imperfections in the level hard to achieve in MRI. Therefore, reference values

using NMR spectroscopy can greatly strengthen the reliability of the phantom. The measurements were performed at NIST using a 3T system (Tecmag Redstone with Doty Scientific 5 mm probe) on single material sample tubes. IR T_1s with composite inversion pulses were measured with 20 logarithmically spaced inversion times. T_2s were measured using a spin-echo sequence with 20 linearly spaced echo times. $T_{1\rho}$ sequences used a spin-lock-prepared sequence with 20 times of spinlock using spin lock frequences of 300, 400, 500, 1000, 2000, and 5000 Hz. Each sequence was adjusted to ensure full coverage of the relaxation range over the timing array. All measurements were allowed for sufficient recovery (TR > $5T_1$). All measurements were measured at six degrees ranging 16°C-26°C, with an increment of 2°C. The NMR and MRI measurements were compared in linear regression plot, Bland-Altman plot, as well as CV to evaluate the accuracy of the MRI measurements regarding the reference value provided by the NMR measurement.

V.3 RESULTS

V.3.1 Longitudinal Stability of MRI measurements
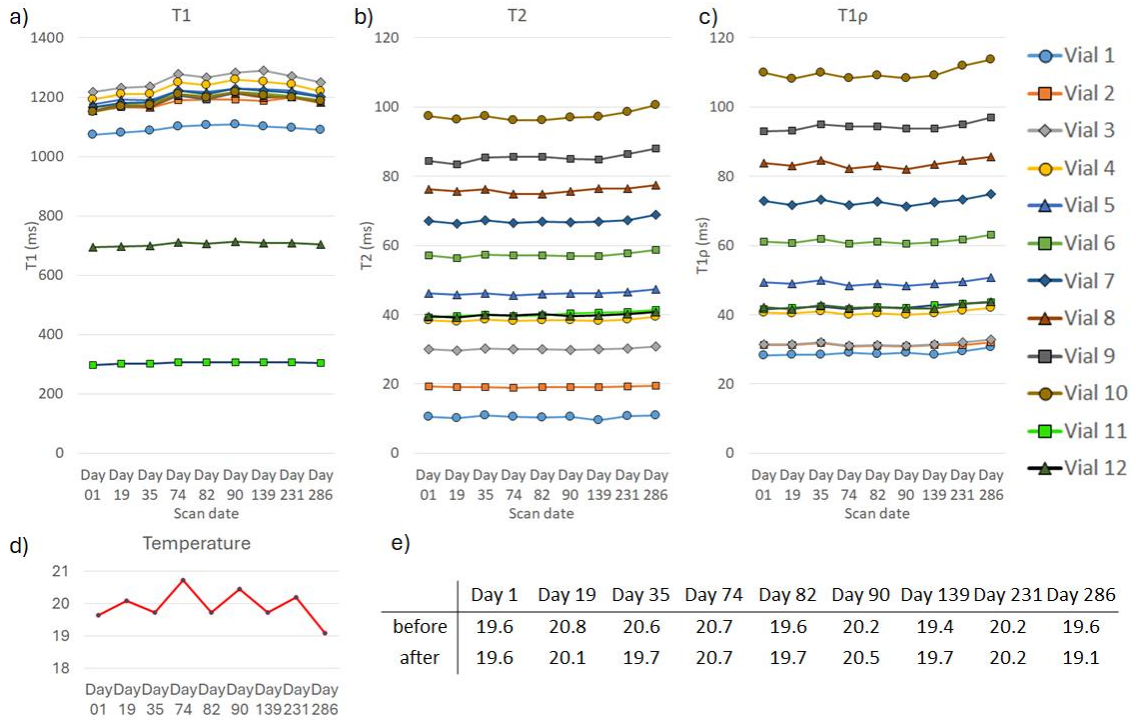
Figure 22 Longitudinal measurement of MRI a) T_1, b) T_2, c) $T_{1\rho}$ for prototype phantom created from the first batch along with the d, e) temperature measurement.

Figure 22 shows the MRI T_1, T_2, and $T_{1\rho}$ measurement from prototype phantom created from the first batch over 9-month period. The measurements were very stable, with longitudinal CV under 2 % for all measurements (1.5±0.4 % for T_1, 1.4±0.8 % for T_2, and 1.6±0.3 % for $T_{1\rho}$). The temperature distribution of the measurements was 20.3±0.99 ºC.

V.3.2 Intra- Inter-Batch Repeatability
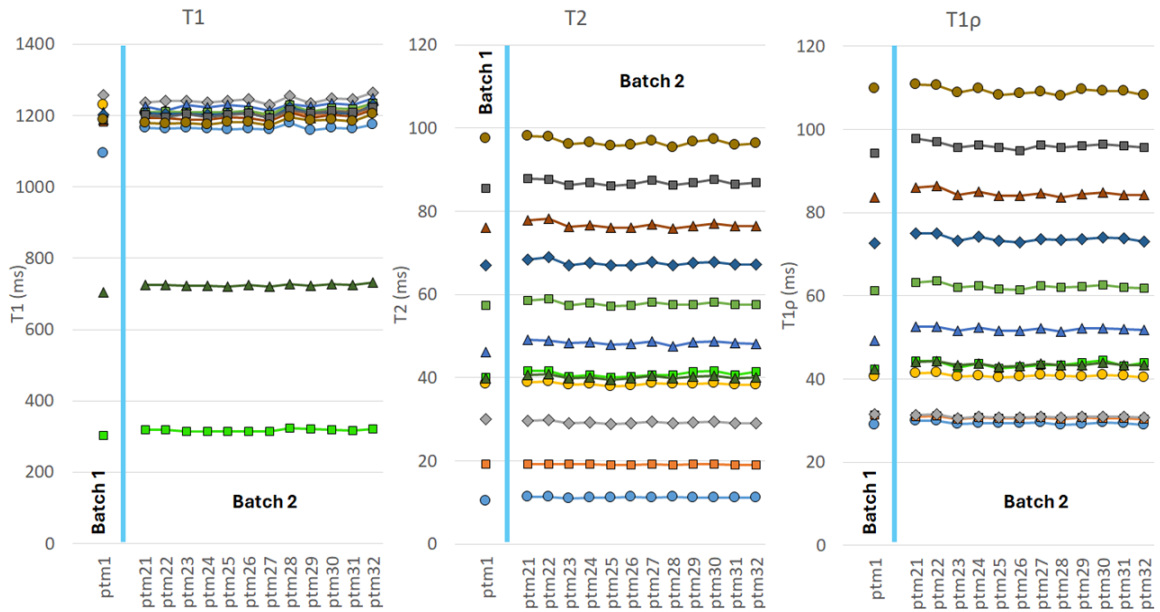
Figure 23 MRI T_1, T_2, $T_{1\rho}$ measurements for 12 phantoms created in the second batch.

Figure 23 MRI T_1, T_2, and $T_{1\rho}$ measurement from the 12 phantoms created in the second batch. The intra-batch CVs were under 1 % for all measurements (0.89±0.23 % for T_1, 0.7±0.18 % for T_2, and 0.84±0.21 for $T_{1\rho}$). Inter-batch CVs between the two batches were under 2 % for all measurements (1.4±1.1 % for T_1, 1.2±1.4 % for T_2, and 1.3±0.8 for $T_{1\rho}$).

V3.3 MRI Measurement Inter-Vendor Reproducibility
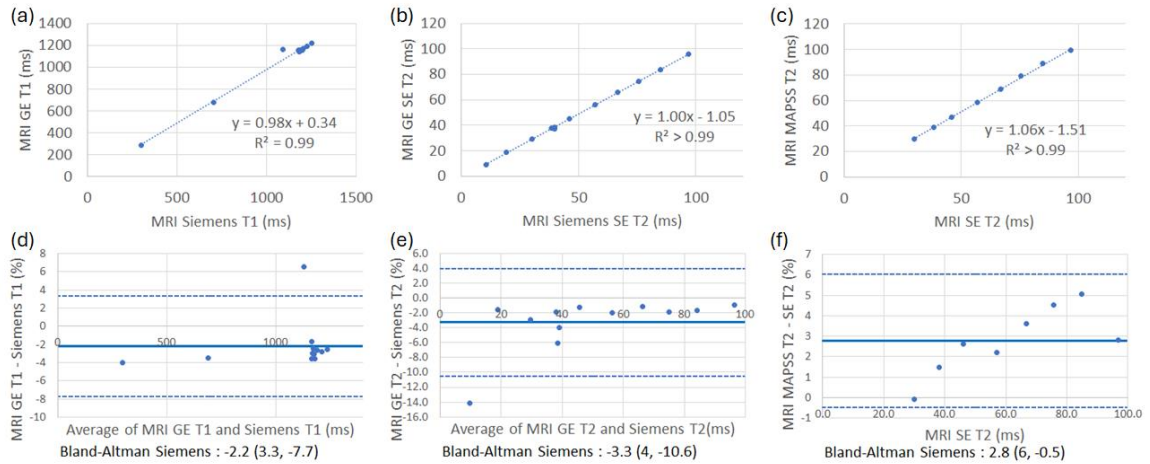
Figure 24 Linear regression (top row) and Bland-Altman plot (bottom row) between two MRI scanner (GE, Siemens) measurements in (a, d) T1 and (b, e) T2. Both measurements agree well between different scanners. (c, f) shows the difference between SE T2 and MAPSS T2 in Siemens scanner. Four outliers were exempt from the comparison, two with short T2 (Vial 1, 2) and two with high B0 and B1 inhomogeneity (Vial 11, 12).

Figure 24 shows the comparison of different MRI measurements. Between the measurements from GE and Siemen scanners, both T_1 and T_2 agreed well with each other, with the linear regression close to unity and R^2 close to 1 (Figure 24a, b). Measurements had average normalized difference of 2.2 % for T_1 and 3.3 % for T_2 (Figure 24d, e). SE T_2 was also close to MAPSS T_2, linear regression close to unity and R^2 close to 1 (Figure 24c). SE T_2 had average normalized difference of 2.8 % with MAPSS T_2, with increasing difference at higher T_2.

V3.4 NMR Measurements and Comparison with MRI Measurements
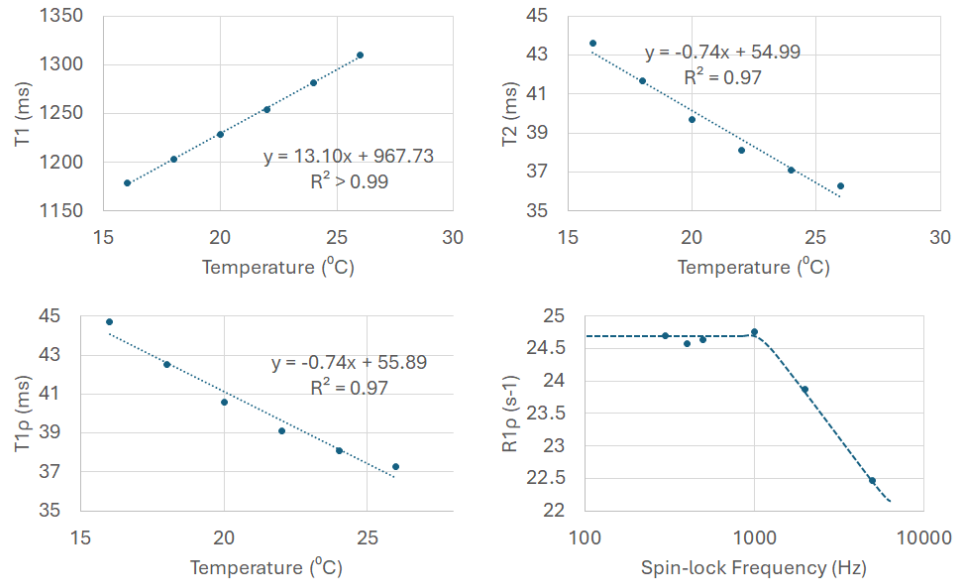
Figure 25 NMR measurements of Vial 4 with different temperature (16~26 ℃) and $R_{1\rho}$ with different spin lock frequency at 20 ℃ (300 – 5000 Hz). Such measurement can be used to correct for the temperature dependency of the relaxation time.

Figure 25 shows a sample NMR measurement from Vial 4 with different temperature and different spin lock frequency. The measurements show expected trend on increasing T_1, decreasing T_2 and $T_{1\rho}$ with increase of temperature. $R_{1\rho}$, inverse of $T_{1\rho}$, increased with increase of spin-lock frequency, which also conforms with the physics.
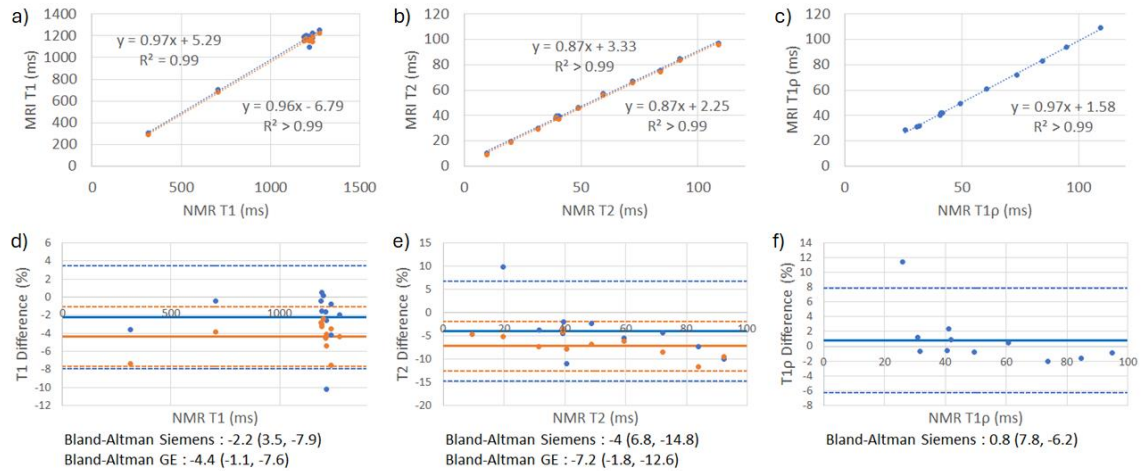
Figure 26 Linear regression (top row) and Bland-Altman plot (bottom row) between NMR and MRI measurements in (a, d) T_1, (b, e) T_2, and (c, f) $T_{1\rho}$. Blue markers are for Siemens MRI, and orange markers are for GE MRI. T_1 and $T_{1\rho}$ agrees well between the NMR and MRI measurements, whereas T_2 was underestimated significantly in MRI.

Figure 26 shows the comparison between the NMR and MRI measurements for T_1, T_2, and $T_{1\rho}$. Both GE and Siemens MRI measurements were close to NMR measurements in T_1 and $T_{1\rho}$, with linear regression line close to unity and average normalized difference of -2.2 % for Siemens T_1, -4.4 % for GE T_1, and -0.2 % for Siemens $T_{1\rho}$. On the other hand, T_2 was underestimated in MRI compared to NMR, with average difference of -5.3 % for Siemens T_2, and -7.2 % for GE T_2.

V.4 DISCUSSION

In this study, the MSK Relaxometry Phantom was developed and evaluated with MRI and NMR measurements in multiple aspects. This MSK-dedicated phantom will greatly facilitate the development and standardization of qMRI assessment.

The design aspects that were included in developing the phantom greatly helped throughout the experiment from data collection to image processing. With the help of the

phantom stands designed for most used knee coils, the placement of the phantom was consistent without extensive care during the positioning. Since the curvature of the phantom stand that matches the interior of the RF coil, placement of the phantom naturally moved the phantom and the phantom stand to the best fit by the weight placed on the curvature. Notch on the phantom stand and the slot on the phantom also locked the phantom so either strict sagittal or coronal planes would cut through the vials perpendicularly. The phantom stand was designed to place the phantom close to the center of the coil, and this led to relatively homogeneous receive and transmit of the RF throughout the phantom. Moreover, liquid filling the phantom helped the B_0 and B_1 shimming process by providing signal in a larger space encompassing the vials. These factors combined led to highly consistent data collection, which helped reduce the influence of inconsistencies in phantom placement and imaging volume rotation.

During the image processing, MRI-visible thermometer greatly helped the logistical problem when trying to track the temperature of the phantom during the time of acquisition. Since the MRI images that includes the temperature readings are collected alongside the other MRI images collected for relaxometry quantification, it removed the need of the person conducting the scan visually reading, recording, and passing the information. Also, the record was easier to reconcile since one would only need to measure the temperature from the image again. These temperature readings can be used to remove the temperature-related error when comparing the acquisition accuracy between different sites when used with the temperature dependency curve measured with NMR (Figure 25). In this study, temperature corrections were not used for the longitudinal acquisition since the temperature distribution was too narrow (20.3±0.99 ºC) that the temperature correction

led to increased variability. The correction is expected to be critical if the temperature measurements are at least 3 ⁰C since this temperature difference leads to over 5 % change in relaxation time measurements (~2 % change in relaxation times with 1 ⁰C difference, Figure 25). Temperature difference below that will likely be obscured by the scan-rescan variability of the acquisition.

With these features, the longitudinal measurements collected from the prototype phantom were very stable, with less than 2 % longitudinal CV over a 9-month period. Such longitudinal stability ensures that the phantom scans during long studies such as studies that acquire follow-up scans will help track the scanner's performance during the time. Furthermore, change of scanners related to maintenance, hardware or software, are likely to occur during long study period. This stable phantom can be used to track and minimize the difference caused by such changes by comparing the scans performed before and after.

The manufacture process of the phantom was also evaluated through intra- and inter-batch comparison of different phantoms. The production was highly repeatable, with intra-batch variability less than 1 % for all MRI measurements and inter-batch variability less than 2 %. This makes sure the measurements performed on the same make of this phantom can be directly compared without expecting large variations between phantoms, and results from different research can be compared and interpreted easier when those works include evaluations using this phantom.

During the selection of imaging sequences for relaxometry quantification, we selected the acquisitions that were accepted as gold standard, which was IRSE for T_1 and SE for T_2. Minimum turbo factors were used for T_1, and just single spin echo was used for T_2. Single slice imaging was used especially for T_1 measurement since the imperfect slice

selection profile of the inversion pulses can lead to slice crosstalk related T_1 error, and can be difficult to account for especially when the different vendors utilize different RF pulse design. With this effort, comparison of MRI measurements between different vendors in T_1 and T_2 showed the measurements agreed well with each other with less than 5 % normalized difference (Figure 24a, b, d, e). MAPSS T_2 was close to SE T_2 with less than 5 % normalized difference, but with interesting trend of increased overestimation of MAPSS T_2 compared to SE T_2 with increase of T_2 (Figure 24c, f). This trend will be explained when comparing the NMR and MRI T_2 measurements.

The NMR measurements provided with the phantom increases the value of the phantom since it provides the ground truth during the development of relaxation time quantification methods. MRI T_1 and $T_{1\rho}$ measurements were close to the NMR measurements, with normalized difference less than 5 %. NMR $T_{1\rho}$ also showed the dispersion effect in high SLF. However, T_2 was significantly underestimated in MRI compared to NMR. One of the possible factors of this discrepancy is the diffusion related signal decay during the MRI acquisition. MRI pulse sequence includes gradient fields superimposed on the imaging volume during the scan. Such gradient fields can act as a diffusion weighting gradient and cause the measured T_2 decay faster than it should be. The magnitude of effect for this factor was not evaluated, but the reduction of SE T_2 compared to MAPSS T_2 can be related to this diffusion effect since MAPSS T_2 uses nonselective inversion during the magnetization preparation without gradient field and multiple inversion pulses also work as a factor to reduce the diffusion related T_2 reduction. Further investigation is warrant for this discrepancy.

In conclusion, we were able to develop a longitudinally stable and reproducible MSK Relaxometry Phantom. Many design features such as phantom stand, built-in MR-visible thermometer, and NMR measurements with temperature control for reference value strengthens its functionality in qMRI research for MSK.

V.5 ACKNOWLEDGMENTS

CHAPTER VI: ACCELERATED T1ρ IMAGING FOR KNEE CARTILAGE IN 3 MINUTES: COMPARISON OF COMPRESSED SENSING AND DEEP LEARNING RECONSTRUCTION

VI.1 INTRODUCTION

One major hurdle in using $T_{1\rho}$ imaging is the prolonged scan time due to the need for multiple images to produce a $T_{1\rho}$ map. Such long scan times decrease efficiency of patient care and thus increase cost, and potentially increase patient discomfort and motion artifacts, making $T_{1\rho}$ imaging technique clinically impractical.

To accelerate the acquisition, parallel imaging techniques have been developed that take advantage of multi-channel coils that allow MRI reconstruction from k-space data sampled below the Nyquist sampling rate.[55-58] However, the scan time, even with the parallel imaging acceleration, was typically longer than 10 minutes for the 8 echo acquisitions needed for $T_{1\rho}$ imaging covering the whole knee,[50] and the techniques could not achieve higher acceleration factors while keeping quantitative accuracy.

To achieve higher acceleration factors, various reconstruction algorithms were developed using Compressed Sensing (CS) and more recently using Deep Learning (DL). In CS, regularized reconstruction from undersampled k-space is performed using intrinsic sparsity of the image. Zibetti et al. compared 12 different sparsifying transforms in CS to accelerate 3D-$T_{1\rho}$ imaging and suggested that spatial-temporal finite-difference (STFD) regularization had the best results with acceleration factor up to 10 and $T_{1\rho}$ errors of 5.1%.[32]

DL reconstruction research has flourished in the recent years, yielding excellent results in wide variety of imaging methods. Its ability to capture highly non-linear

relationships in the data hard to analytically model and solve by human and fast reconstruction time after the long training are the major appealing factors of the method. With collaboration with Dr. Leslie Ying, we developed SuperMAP, which is a DL reconstruction model for 3D $T_{1\rho}$ and T_2 imaging, which achieved 2.7 % nRMSE error at acceleration factor (AF) 24 and 2.8 % at AF 32.[59]

Previous work with these CS and DL reconstruction and its evaluation has been limited to retrospective data undersampling, which creates the undersampled data by picking data points from fully sampled k-space and is different from actual scans with prospective undersampling. Therefore, it is important to evaluate the reconstruction algorithm prospectively undersampled dataset. It is especially important with $T_{1\rho}$ imaging, since these sequences are magnetization-prepared acquisitions that collect multiple k-space samples after a single $T_{1\rho}$ preparation, and thus k-space weighting could be changed between retrospective and prospective downsamplings. Furthermore, no previous studies have evaluated CS or DL $T_{1\rho}$ imaging in patients with degenerated cartilage and compared their performance.

The goal of this study was to evaluate the application of fast cartilage $T_{1\rho}$ imaging STFD regularized CS reconstruction and SuperMAP DL reconstruction, and to evaluate its reliability and repeatability using retrospective and prospective downsampling in subjects with and without OA. Side-by-side comprehensive comparison of the two reconstruction methods were conducted.

VI.2 METHODS

VI.2.1 Sequence Setup

3D MAPSS sequence was used for both reference and prospectively undersampled $T_{1\rho}$ imaging. The points of sampling mask in the k-space were sorted in an ascending order based on the distance from the center of k-space. According to this order, a fixed number of samples, noted as views per segment, were collected after every preparation. The samples were spaced by the number of shots required to fill a k-space, resulting in center-out k-space ordering. The same methodology was used with prospectively undersampled acquisition. The sampling masks were different between $T_{1\rho}$-weighted images with different TSLs to accommodate different spatial information in different echoes but were fixed for all scans to avoid variation due to change of sampling mask. The sampling mask was generated by a 2D variable-density random pattern along the phase encoding and slice encoding directions.[60] The center k-space was fully sampled to get low-resolution coil sensitivity used for STFD reconstruction, and the outer k-space was sparsely sampled using an exponential probability distribution function.

VI.2.2 Volunteer Scans

Volunteer scans were performed with a 3T MR scanner (Magnetom Prisma, Siemens Healthcare AG, Erlangen, Germany) with a 1Tx and 15Rx knee coil (QED, Mayfield, OH). Nine volunteers were scanned. All procedures were approved by the Institutional Review Board (IRB). Two healthy volunteers were scanned once, and four healthy volunteers and three volunteers with diagnosed pathologies were scanned twice, with repositioning between the scans. For SuperMAP, 4 knees from 3 volunteers separate

from the previous 9 volunteers with scan and rescan were used for training and excluded

from comparisons. For imaging sequences, 8 echo 3D MAPSS was used for $T_{1\rho}$ imaging,

and dual-echo steady-state (DESS) was collected for cartilage segmentation. $T_{1\rho}$ images

were collected four times with different acceleration. For reference, GRAPPA factor 2 was

used. Images with acceleration factors (AF) of 4, 6, and 8 were collected. Note that the

accelerated scans were prospectively undersampled, meaning all scans were performed

separately. Table 5 shows detailed sequence parameters.

Sequence	TR/TE (ms)	FOV (mm^2)	Matrix	Slice thickness (mm)	Acceleration	Bandwidth (Hz)	Acquisition Time
DESS	17.55/6.02	140x140	384x307x160	0.7	GRAPPA 2	185	5:56
3D MAPSS		140x140	320x160x24	4	See below	390	See below
Other parameter for MAPSS		Spin-lock Frequency = 500 Hz, number of echoes = 8, T_1 recovery time = 1.5 s, TSL = [0 10 20 30 40 50 60 70] ms **Reference:** GRAPPA 2, views per segment = 92, # of shots/echo = 24, total acquisition time = 13:43 **AF 4 :** views per segment = 80, # of shots/echo = 12, total acquisition time = 6:37 **AF 6 :** views per segment = 80, # of shots/echo = 8, total acquisition time = 4:24 **AF 8 :** views per segment = 80, # of shots/echo = 6, total acquisition time = 3:18						

Table 5 Imaging sequence parameters

VI.2.3 Image Processing

Collected volunteer data were reconstructed using STFD CS reconstruction and

SuperMAP DL reconstruction. For STFD CS reconstruction, all 8 echoes were used for

reconstruction with AF 8. Regularization factor was optimized using one phase-slice

encoding slice of the first volunteer, and same regularization factor was used for all subjects.

For SuperMAP DL reconstruction, the model was trained on separate training data using

retrospectively undersampled images from separate cohort, as explained in VI.2.2, using 4

echoes (0, 10, 30 ,70 ms) with each echo undersampled by 4, resulting in overall AF 8.

Retrospective reconstruction was performed by subsampling GRAPPA-reconstructed k-

space of reference data using the same sampling mask used in prospectively undersampled

data. For reference, multi-coil data was combined using complex-coil-combination using coil sensitivity map. The DESS images were non-linearly registered to the first echo of $T_{1\rho}$-weighted images using ANTS.[31] After registration, DESS images were processed with automatic cartilage segmentation using a deep learning network developed in house.[49] Six cartilage compartments were segmented, which included the medial/lateral femoral condyle (MFC/LFC), medial/lateral tibial (MT/LT), trochlear (TRO), and patellar (PAT) cartilage.

For evaluation of retrospective reconstruction result, no registration was applied in both reference and CS reconstruction to avoid manipulation of image from registration algorithm. There was no need for registration for DL reconstruction since SuperMAP outputs the $T_{1\rho}$ map directly. To compare with accelerated maps, $T_{1\rho}$ map was created using 2 echo (TSL = 0, 70 ms) out of 8 echo reference acquisition to see if simply using smaller number of echoes can achieve better result compared to advanced reconstruction methods. $T_{1\rho}$ images were fitted with mono-exponential fitting using the Levenberg-Marquardt algorithm to produce $T_{1\rho}$ maps.[61, 62] For voxel-wise evaluation between reference and retrospectively reconstructed map, median normalized absolute difference (MNAD) was calculated between the reference and accelerated maps in cartilage compartments.[32] CVs and concordance correlation coefficients (CCCs) were calculated using mean $T_{1\rho}$ values of each compartment among the reference map and the maps with different acceleration factors. Pixel-wise value-based scatter plot and compartment average value-based Bland-Altman analysis between different combinations of reference and accelerated maps was used to better visualize the results.

For prospective reconstruction evaluation, reconstructed $T_{1\rho}$-weighted images from CS reconstruction were linearly registered among the echoes using ANTS and fitted using the Levenberg-Marquardt algorithm to produce $T_{1\rho}$ maps. Similar analysis as in retrospective reconstruction was done except for voxel-wise evaluations. CVs and CCCs were calculated using mean $T_{1\rho}$ values of each compartment between reference and the accelerated maps for reliability of reconstruction algorithm, and between scan and rescan for repeatability. Also, compartment average value-based Bland-Altman analysis was used to better visualize the results.

VI.3 RESULTS

VI.3.1 Retrospectively and Prospectively Accelerated $T_{1\rho}$ Imaging
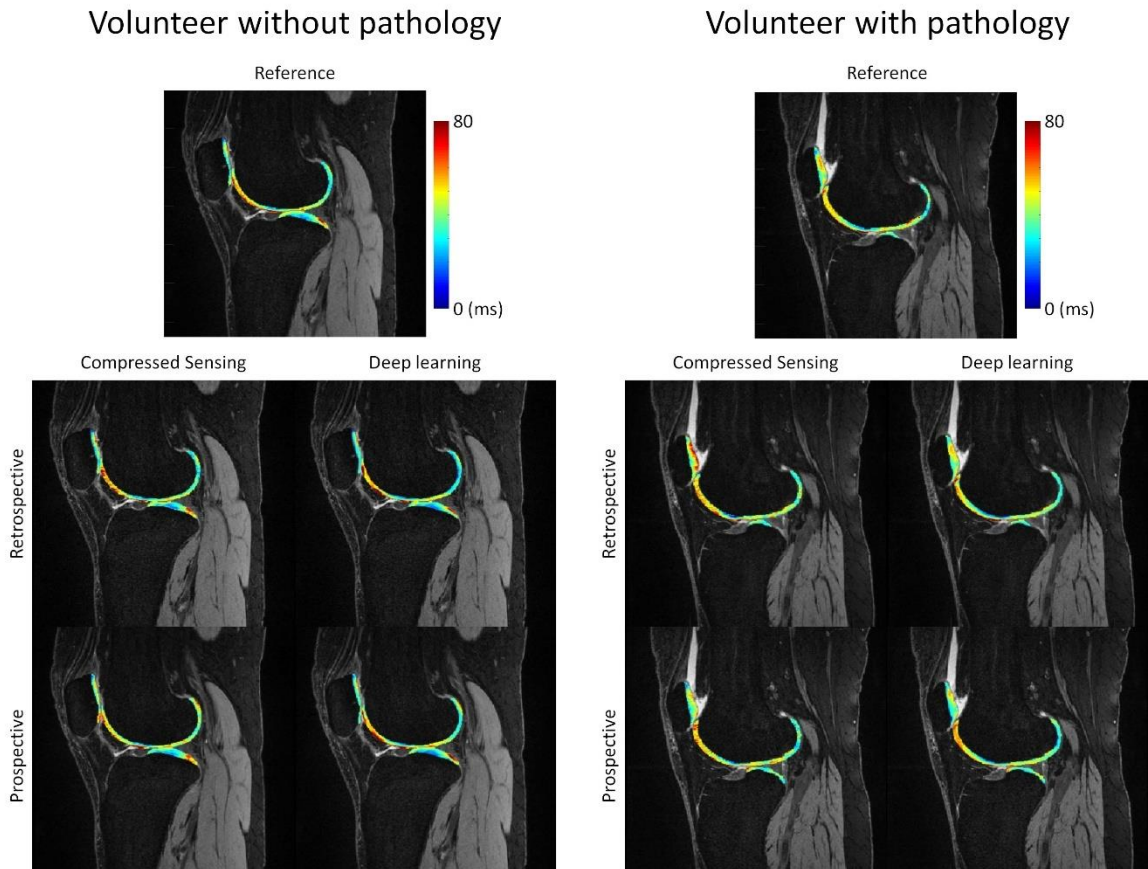
Figure 27 Example image of retrospective and prospective reconstructed images in volunteer without or with pathology.

Figure 27 shows an example slices from retrospective and prospective reconstructed $T1\rho$ maps in volunteers without or with pathology. Both CS and DL reconstructed maps were able to preserve fine details in both reconstructions regardless of the pathology.

VI.3.2 Comparison Between Retrospectively Accelerated and Reference $T_{1\rho}$ Imaging
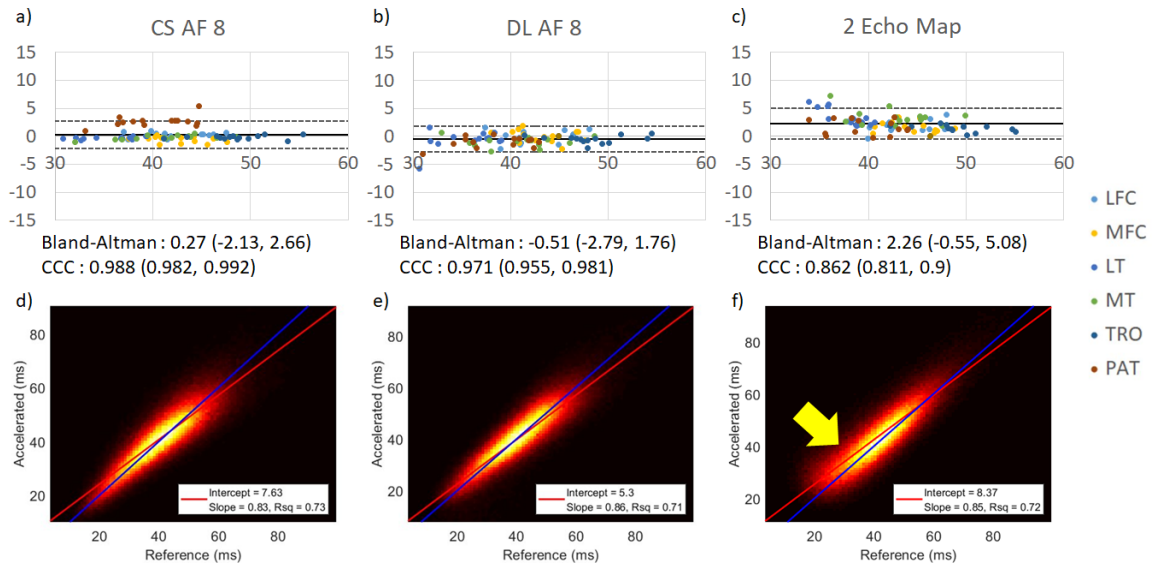
Figure 28 Bland-Altman plot (top row) and voxel-wise scatter plot (bottom row) between reference and retrospectively-undersampled a, d) CS reconstruction and b, e) DL reconstruction. c, f) was the comparison between 8 echo reference map and map created from 2 echo of the 8 echo reference images. Both CS and DL reconstruction shows good agreement in Bland-Altman plot and voxel-wise scatter plot and outperforms the map created from 2 echoes.

Top row of Figure 28 shows the Bland-Altman plot created from the average values of cartilage each cartilage compartments. Both CS and DL reconstruction (Figure 28a, b) shows good agreement between the reference map and accelerated map, with mean bias less than 0.5 ms and CCC close to 1. However, $T_{1\rho}$ values from PAT showed consistent overestimation unlike other cartilage compartments in CS reconstruction. Bland-Altman plot and CCC both showed worse result when comparing map created from 2 echoes of reference images (Figure 28c) and CS or DL reconstructed map.

Bottom row of Figure 28 shows the voxel-wise scatter plot between reference and accelerated maps. Similar too Bland-Altman plot, the regression line shows that DL and CS accelerated maps (Figure 28d, e) agree well with the reference map. The map created from two echoes of the reference images (Figure 28f) all showed worse results compared to CS or DL reconstruction. Moreover, the maps showed prevalent overestimation in lower $T_{1\rho}$ value (indicated by yellow arrow), which most likely coming from fitting a map with low SNR image.

a) CV (%) calculated from compartment average value

Method	LFC	MFC	LT	MT	TRO	PAT	All
CS AF 8	0.8	1.0	0.6	0.6	0.4	4.6	1.4
DL AF 8	1.6	1.5	2.2	1.9	1.0	2.1	1.7
2 Echo Map	3.2	2.8	6.7	5.8	2.1	3.0	3.9

b) MNAD (%) calculated from voxel-wise value

Method	LFC	MFC	LT	MT	TRO	PAT	All
CS AF 8	9.9	10.4	8.7	9.7	9.6	11.1	9.9
DL AF 8	9.7	9.8	10.3	10.7	8.7	9.4	9.8
2 Echo Map	11.0	10.6	12.6	12.4	8.3	9.5	10.7

Table 6 Retrospective reconstruction results

Table 6a shows CVs between reference and accelerated $T_{1\rho}$ imaging values in each defined cartilage compartment of volunteers. Average CV between the reference and the prospectively accelerated relaxation map was under 3% in both CS and DL reconstruction regardless of pathology, thus showing excellent agreement between the maps. The result did not change with or without pathology (average CV 1.4, 1.5% for CS, DL reconstruction without pathology, respectively, average CV 1.2, 2.2 % for CS, DL reconstruction with pathology). Among the cartilage compartments, the CV in the patella cartilage showed highest CV. Similar to previous results, 2 echo created maps showed worse results. Voxel-wise MNAD also showed the same trend in all aspects.

VI.3.3 Comparison Between Prospectively Accelerated and Reference $T_{1\rho}$ Imaging

CS AF 8

DL AF 8

- LFC
- MFC
- LT
- MT
- TRO
- PAT

Bland-Altman : 1.77 (-3.85, 7.39)
CCC : 0.754 (0.661, 0.823)

Bland-Altman : 0.2 (-3.06, 3.45)
CCC : 0.939 (0.908, 0.959)
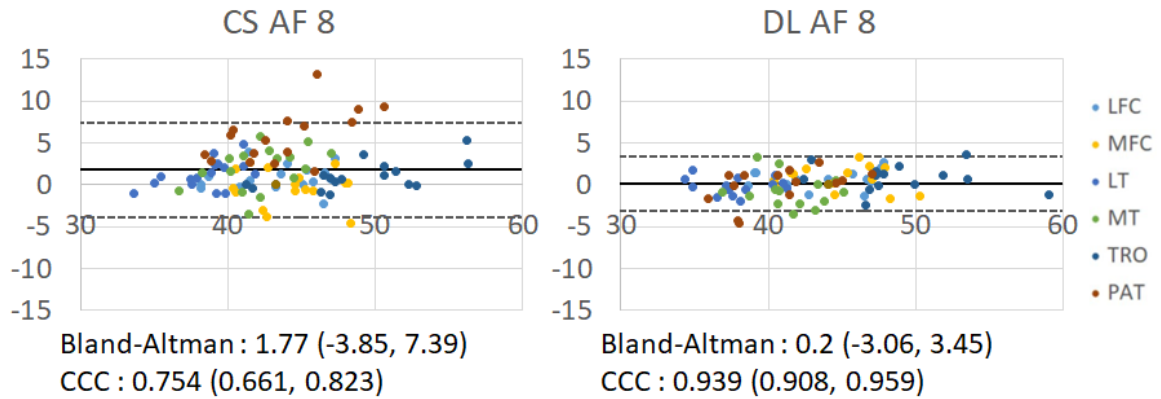
Figure 29 Bland-Altman plot between reference and prospectively undersampled reconstruction. Both reconstructions suffered degradation of evaluation metric compared to retrospective reconstruction. However, the CS reconstruction suffered greater degradation compared to DL.

Figure 29 shows the Bland-Altman plot for the prospective reconstruction. Compared to retrospective reconstruction, all metrics showed worse result in both prospective reconstructions (Figure 28a, b). Among the two, CS reconstruction suffered worse degradation, and systematic bias was created between the reference and accelerated map. PAT cartilage showed larger overestimation compared to other compartments, which was also seen from the retrospective reconstruction result.

a) All volunteers

CV (%)	LFC	MFC	LT	MT	TRO	PAT	All
CS AF 8	2.0	2.6	3.0	4.6	1.9	9.2	3.9
DL AF 8	2.3	2.4	1.3	2.7	2.7	3.1	2.4

b) Volunteers without pathology

CV (%)	LFC	MFC	LT	MT	TRO	PAT	All
CS AF 8	2.0	2.9	3.1	4.4	1.9	7.6	3.7

DL AF 8	2.8	2.1	1.3	3.2	3.1	3.5	2.6

c) volunteers with pathology

CV (%)	LFC	MFC	LT	MT	TRO	PAT	All
CS AF 8	1.9	1.9	2.8	4.9	1.9	11.9	4.2
DL AF 8	1.4	2.8	1.5	1.5	1.9	2.3	1.9

Table 7 CV (%) between reference and prospective reconstruction result

Table 7 shows the CVs calculated between the reference and prospective reconstruction result. Similar to the Bland-Altman plot, both reconstructions performed worse than retrospective reconstruction (Table 6a), and worse degradation for CS reconstruction. Interestingly, PAT cartilage showed the worst result in CS reconstruction, and showed worse result in volunteers with pathology compared to without. Apart from PAT cartilage, all other cartilage compartments showed less than 5 % CV.

Ref	CS AF 8	DL AF 8
Bland-Altman : -0.05 (-4.23, 4.13)	Bland-Altman : 0.22 (-4.03, 4.48)	Bland-Altman : 0.33 (-3.23, 3.89)
CCC : 0.891 (0.808, 0.939)	CCC : 0.907 (0.835, 0.948)	CCC : 0.917 (0.84, 0.958)
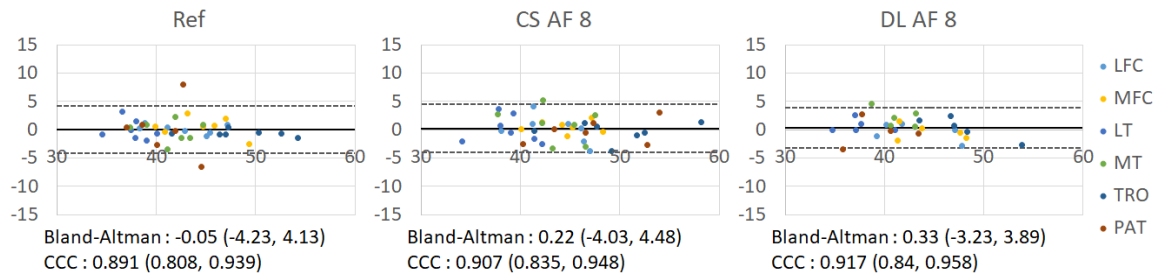
Figure 30 Bland-Altman plot between scan-rescan with reference imaging and prospective reconstruction.

a) All volunteers

	LFC	MFC	LT	MT	TRO	PAT	All
Reference	1.06	2.58	2.61	3.33	1.62	4.20	2.57
CS AF 8	2.88	1.42	3.66	4.44	1.72	2.62	2.79
DL AF 8	1.94	1.91	1.39	3.77	2.37	2.38	2.29

b) Volunteers without pathology

	LFC	MFC	LT	MT	TRO	PAT	All
Reference	0.89	2.85	1.87	4.23	1.68	1.60	2.19
CS AF 8	3.41	1.07	3.74	4.74	2.22	2.17	2.89
DL AF 8	2.02	2.16	1.73	4.48	2.66	2.73	2.63

c) Volunteers with pathology

	LFC	MFC	LT	MT	TRO	PAT	All
Reference	1.27	2.21	3.60	2.13	1.54	7.68	3.07
CS AF 8	2.17	1.90	3.55	4.03	1.05	3.22	2.65
DL AF 8	1.60	0.90	0.04	0.94	1.18	0.99	0.94

Table 8 Scan-rescan CV (%) in reference imaging and prospective reconstruction

Figure 30 shows the scan-rescan repeatability of the reference imaging and prospective reconstruction. The accelerated maps showed excellent repeatability using either CS or DL reconstruction with CV<5% for all compartments and average CV<3% regardless of the pathology, similar to the reference imaging.

VI.4 DISCUSSION

In this study, we evaluated CS reconstruction with STFD regularization and SuperMAP DL reconstruction. The retrospective reconstruction showed excellent agreement compared to reference and prospective reconstruction showed excellent scan/rescan repeatability for both reconstruction methods. The prospective reconstruction showed worse performance compared to retrospective reconstruction, and worse degradation was achieved by CS reconstruction.

Both retrospective CS and DL reconstruction showed better result than using fewer echoes from the reference imaging. The overestimation coming from fitting images with low SNR agrees with the what was previously reported, and complex-combination could not fully resolve the problem. The larger CV in MT and LT is also evidence to the noise-related overestimation, since these compartments had lower SNR and shorter $T_{1\rho}$ values compared to other compartments. Moreover, using fewer number of echoes could lead to bigger discrepancy with B_0 or B_1 inhomogeneities, as introduced in Chapter IV, which

could negatively affect the reproducibility of the method between different sites and vendors.

Volunteer scan results showed excellent agreement between reference and retrospectively accelerated $T_{1\rho}$ imaging, with CVs <2% for all compartments other than the PAT for CS reconstruction. These CVs were much less than scan-rescan repeatability of the reference $T_{1\rho}$ imaging in this study and the reported repeatability of standard $T_{1\rho}$ imaging in the literature. The result also did not have a significant bias between the reference and accelerated maps. Furthermore, the presence of pathology did not impact the performance of the reconstruction algorithm, meaning that the lesions with abnormally high $T_{1\rho}$ values were well-preserved with both reconstruction algorithms. The voxel-wise average MNAD less than 10% for both reconstruction algorithms.

Overall, the prospective reconstruction showed excellent scan-rescan repeatability in both reconstruction methods. The scan-rescan CVs were comparable to that of reference scan, with mean CV less than 4% in both methods. However, the Bland-Altman plot between reference and accelerated maps in Figure 29 showed larger difference than in retrospective reconstruction (Figure 28a, b). The difference was especially larger in CS reconstruction compared to DL reconstruction. Among the cartilage compartments, PAT cartilage had the worst result, and even bigger difference could be observed in volunteers with pathology (CV 7.6 % without pathology, 11.9 % with pathology in Table 7). However, average CVs decreases to 2.8 % overall when excluding PAT cartilage from calculation, which is similar to scan-rescan repeatability. After excluding the PAT cartilage, there are no significant difference between CVs with or without pathology (2.9 % without pathology, 2.7 % with pathology).

There is one possible explanation for PAT cartilage showing higher CVs with respect to the reference map using prospective reconstruction than that using retrospective reconstruction, especially in cases with pathology. In general, all volunteers had synovial fluid located near the patella, and even more pronounced in volunteers with pathology. Fluid in this position tends to be mobile, often leaving a hollow region in the rescan, or vice versa. Sample images are shown in Figure 31.
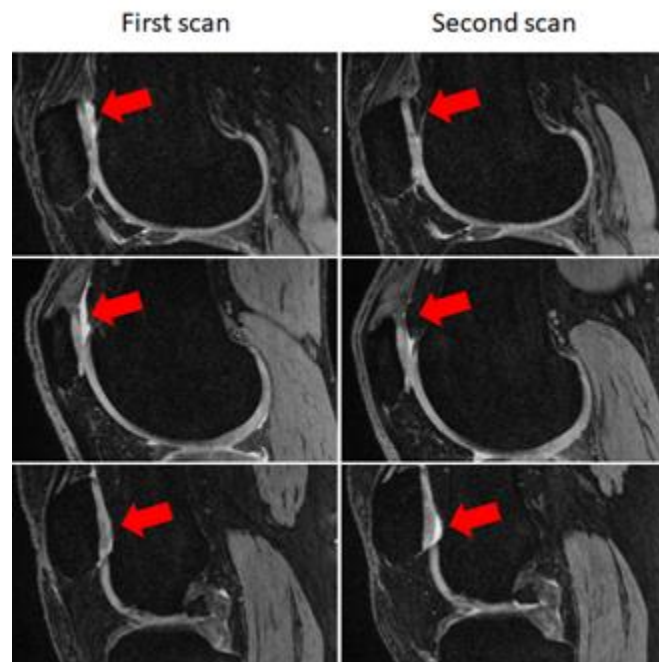
Figure 31 DESS image of scan and rescan where synovial fluid near PAT cartilage changed with time.

This not only made the registration between $T_{1\rho}$ images and DESS challenging, but also raises the possibility of actual change in $T_{1\rho}$ value in patella cartilage due to partial volume averaging. This could explain the higher reference to accelerated map CV in PAT for volunteers with pathology compared to volunteers without pathology (Table 7) and higher scan-rescan CV in reference $T_{1\rho}$ map (7.68 % in Table 8c) compared with CS reconstruction in subjects with pathology (3.22% in Table 8c). The scans were ordered in

DESS, reference $T_{1\rho}$ imaging, AF 4, 6, and 8. The volunteer was on the scanner table for approximately 10 and 50 minutes for scan and rescan of reference $T_{1\rho}$ imaging, and 35 and 75 minutes for scan and rescan of AF 8. If the fluid near the patella cartilage relocated during the 30 minutes of unloading, it could explain the higher scan-rescan CV of reference $T_{1\rho}$ imaging; the fluid did not fully relocate in the first reference T1ρ imaging. This phenomenon was more prominent for volunteers with pathology, since these volunteers tended to have more fluid and thinner patella cartilage. However, more cases are needed to validate this assumption.

In conclusion, DL reconstruction was favorable over CS reconstruction. Although both had good retrospective reconstruction result, DL reconstruction was able to preserve the reconstruction performance in prospective reconstruction whereas CS reconstruction. Also, the reconstruction speed of the DL reconstruction was significantly faster than CS reconstruction (few seconds (DL) vs. 20 minutes (CS)), which is another factor that would facilitate clinical application on the scanner. However, due to the small sample size of this study (12 volunteers overall), there is a possibility that DL reconstruction was able to achieve good result by overfitting, so further investigation is needed to verify the generalizability of the DL reconstruction on a larger cohort.

IV. ACKNOWLEDGMENTS

CHAPTER VII: CONCLUSION

This study has developed reliable and fast knee cartilage T_2 and $T_{1\rho}$ mapping techniques which will greatly facilitate clinical translation of such techniques and enhance their accessibility. The multivendor multisite study established the reproducibility benchmark of the state-of-the-art T_2 and $T_{1\rho}$ mapping techniques. Analysis of the results identified areas requiring improvement. B_1 and B_0 inhomogeneity-robust $T_{1\rho}$ preparation schemes were invented to mitigate one of the major components of scanner-to-scanner and patient-to-patient non-biological variability. An MSK dedicated relaxometry phantom was developed to use as a powerful tool to detect the variability and standardize the acquisition. Lastly, acceleration techniques with advanced image reconstruction methods including compressed sensing and deep learning models were implemented and evaluated. Such techniques allowed higher acceleration factors compared to conventional acceleration methods, facilitating efficient data collection that fits into busy clinical schedules, reduces patient discomfort, and minimizes motion artifacts. Collectively, these efforts will significantly enhance the reliability of the T_2 and $T_{1\rho}$ mapping technique, allowing for higher sensitivity for detecting early cartilage degeneration in OA and subtle changes after interventions or treatments. Furthermore, it will greatly facilitate the clinical translation of such techniques to be used in large scale clinical trials as OA imaging markers, and in clinical practice to improve early diagnosis and prognosis of OA. The study was focused on knee cartilage for OA. The developed techniques can be extended to other tissues and other diseases where tissue compositional changes related to macro-molecules (such as proteins) are of interest.

References

1.   Kraus VB, Blanco FJ, Englund M, Karsdal MA, Lohmander LS. Call for standardized definitions of osteoarthritis and risk stratification for clinical trials and clinical use. Osteoarthritis and cartilage. 2015;23(8):1233-41

2.   Cisternas MG, Murphy L, Sacks JJ, Solomon DH, Pasta DJ, Helmick CG. Alternative Methods for Defining Osteoarthritis and the Impact on Estimating Prevalence in a US Population-Based Survey. Arthritis care & research. 2016;68(5):574-80

3.   Ma VY, Chan L, Carruthers KJ. Incidence, prevalence, costs, and impact on disability of common conditions requiring rehabilitation in the United States: stroke, spinal cord injury, traumatic brain injury, multiple sclerosis, osteoarthritis, rheumatoid arthritis, limb loss, and back pain. Archives of physical medicine and rehabilitation. 2014;95(5):986-95.e1

4.   Karsdal MA, Michaelis M, Ladel C, Siebuhr AS, Bihlet AR, Andersen JR, et al. Disease-modifying treatments for osteoarthritis (DMOADs) of the knee and hip: lessons learned from failures and opportunities for the future. Osteoarthritis and cartilage. 2016;24(12):2013-21

5.   Oo WM, Yu SP, Daniel MS, Hunter DJ. Disease-modifying drugs in osteoarthritis: current understanding and future therapeutics. Expert opinion on emerging drugs. 2018;23(4):331-47

6.   Bhosale AM, Richardson JB. Articular cartilage: structure, injuries and review of management. British medical bulletin. 2008;87:77-95

7.   Guermazi A, Alizai H, Crema MD, Trattnig S, Regatte RR, Roemer FW. Compositional MRI techniques for evaluation of cartilage degeneration in osteoarthritis. Osteoarthritis and cartilage. 2015;23(10):1639-53

8.   Link TM, Neumann J, Li X. Prestructural cartilage assessment using MRI. Journal of magnetic resonance imaging : JMRI. 2017;45(4):949-65

9.   Atkinson HF, Birmingham TB, Moyer RF, Yacoub D, Kanko LE, Bryant DM, et al. MRI T2 and T1rho relaxation in patients at risk for knee osteoarthritis: a systematic review and meta-analysis. BMC musculoskeletal disorders. 2019;20(1):182

10.   MacKay JW, Low SBL, Smith TO, Toms AP, McCaskie AW, Gilbert FJ. Systematic review and meta-analysis of the reliability and discriminative validity of cartilage compositional MRI in knee osteoarthritis. Osteoarthritis and cartilage. 2018;26(9):1140-52

11.   Joseph GB, Baum T, Alizai H, Carballido-Gamio J, Nardo L, Virayavanich W, et al. Baseline mean and heterogeneity of MR cartilage T2 are associated with morphologic degeneration of cartilage, meniscus, and bone marrow over 3 years--data from the Osteoarthritis Initiative. Osteoarthritis and cartilage. 2012;20(7):727-35

12.   Prasad AP, Nardo L, Schooler J, Joseph GB, Link TM. T(1)rho and T(2) relaxation times predict progression of knee osteoarthritis. Osteoarthritis and cartilage. 2013;21(1):69-76

13.   Li X, Han ET, Busse RF, Majumdar S. In vivo T(1rho) mapping in cartilage using 3D magnetization-prepared angle-modulated partitioned k-space spoiled gradient echo snapshots (3D MAPSS). Magnetic resonance in medicine. 2008;59(2):298-307

14.   Li X, Pedoia V, Kumar D, Rivoire J, Wyatt C, Lansdown D, et al. Cartilage T1rho and T2 relaxation times: longitudinal reproducibility and variations using different coils, MR systems and sites. Osteoarthritis and cartilage. 2015;23(12):2214-23

15.   Li X, Wyatt C, Rivoire J, Han E, Chen W, Schooler J, et al. Simultaneous acquisition of T1rho and T2 quantification in knee cartilage: repeatability and diurnal variation. Journal of magnetic resonance imaging : JMRI. 2014;39(5):1287-93

16.   Carballido-Gamio J, Link TM, Majumdar S. New techniques for cartilage magnetic resonance imaging relaxation time analysis: texture analysis of flattened cartilage and localized intra- and inter-subject comparisons. Magnetic resonance in medicine. 2008;59(6):1472-7

17.   Jordan CD, McWalter EJ, Monu UD, Watkins RD, Chen W, Bangerter NK, et al. Variability of CubeQuant T1rho, quantitative DESS T2, and cones sodium MRI in knee cartilage. Osteoarthritis and cartilage. 2014;22(10):1559-67

18.   Pedoia V, Li X, Su F, Calixto N, Majumdar S. Fully automatic analysis of the knee articular cartilage T1rho relaxation time using voxel-based relaxometry. Journal of magnetic resonance imaging : JMRI. 2016;43(4):970-80

19.   Welsch GH, Apprich S, Zbyn S, Mamisch TC, Mlynarik V, Scheffler K, et al. Biochemical (T2, T2* and magnetisation transfer ratio) MRI of knee cartilage: feasibility at ultra-high field (7T) compared with high field (3T) strength. European radiology. 2011;21(6):1136-43

20.   Zuo J, Li X, Banerjee S, Han E, Majumdar S. Parallel imaging of knee cartilage at 3 Tesla. Journal of magnetic resonance imaging : JMRI. 2007;26(4):1001-9

21.   Dardzinski BJ, Schneider E. Radiofrequency (RF) coil impacts the value and reproducibility of cartilage spin-spin (T2) relaxation time measurements. Osteoarthritis and cartilage. 2013;21(5):710-20

22.   Balamoody S, Williams TG, Wolstenholme C, Waterton JC, Bowes M, Hodgson R, et al. Magnetic resonance transverse relaxation time T2 of knee cartilage in osteoarthritis at 3-T: a cross-sectional multicentre, multivendor reproducibility study. Skeletal Radiol. 2013;42(4):511-20

23.   Pai A, Li X, Majumdar S. A comparative study at 3 T of sequence dependence of T2 quantitation in the knee. Magnetic resonance imaging. 2008;26(9):1215-20

24.   Matzat SJ, McWalter EJ, Kogan F, Chen W, Gold GE. T2 Relaxation time quantitation differs between pulse sequences in articular cartilage. Journal of magnetic resonance imaging : JMRI. 2015;42(1):105-13

25.   Tanaka MS, Pedoia V, Chandramohan D, Chen W, Li X. Comparison of T1ρ quantification, SNR, and reproducibility in 3D Magnetization-Prepared Angle-Modulated Partitioned k-space Spoiled Gradient Echo Snapshots (3D MAPSS) and 3D Fast Spin Echo (CUBEQuant) techniques. Annual conference of International Society of Magnetic Resonance in Medicine (ISMRM); Apr 22-27; Honolulu, USA2017.

26.   Hennig J, Weigel M, Scheffler K. Multiecho sequences with variable refocusing flip angles: optimization of signal behavior using smooth transitions between pseudo steady states (TRAPS). Magnetic resonance in medicine. 2003;49(3):527-35

27.   Saxena V, D'Aquilla K, Marcoon S, Krishnamoorthy G, Gordon JA, Carey JL, et al. T1rho Magnetic Resonance Imaging to Assess Cartilage Damage After Primary Shoulder Dislocation. Am J Sports Med. 2016;44(11):2800-6

28.   Goto H, Iwama Y, Fujii M, Aoyama N, Kubo S, Kuroda R, et al. A preliminary study of the T1rho values of normal knee cartilage using 3T-MRI. European journal of radiology. 2012;81(7):e796-803

29.   Russell C, Pedoia V, Majumdar S, Consortium A-A. Composite metric R2 - R1rho (1/T2 - 1/T1rho) as a potential MR imaging biomarker associated with changes in pain after ACL reconstruction: A six-month follow-up. J Orthop Res. 2017;35(3):718-29

30.   Klein S, Staring M, Murphy K, Viergever MA, Pluim JP. elastix: a toolbox for intensity-based medical image registration. IEEE transactions on medical imaging. 2010;29(1):196-205

31.   Avants BB, Tustison N, Song G. Advanced normalization tools (ANTS). Insight j. 2009;2:1-35

32.   Zibetti MVW, Sharafi A, Otazo R, Regatte RR. Accelerating 3D-T(1ρ) mapping of cartilage using compressed sensing with different sparse and low rank models. Magnetic resonance in medicine. 2018;80(4):1475-91

33.   Zhu Y, Zhang Q, Liu Q, Wang YX, Liu X, Zheng H, et al. PANDA-T1ρ: Integrating principal component analysis and dictionary learning for fast T1ρ mapping. Magnetic resonance in medicine. 2015;73(1):263-72

34.   Cai C, Wang C, Zeng Y, Cai S, Liang D, Wu Y, et al. Single-shot T2 mapping using overlapping-echo detachment planar imaging and a deep convolutional neural network. Magnetic resonance in medicine. 2018;80(5):2202-14

35.   Foltz WD, Stainsby JA, Wright GA. T2 accuracy on a whole-body imager. Magnetic resonance in medicine. 1997;38(5):759-68

36. Akella SV, Regatte RR, Wheaton AJ, Borthakur A, Reddy R. Reduction of residual dipolar interaction in cartilage by spin-lock technique. Magnetic resonance in medicine. 2004;52(5):1103-9

37. Wang N, Xia Y. Experimental issues in the measurement of multi-component relaxation times in articular cartilage by microscopic MRI. Journal of magnetic resonance (San Diego, Calif : 1997). 2013;235:15-25

38. Chen W. Errors in quantitative T1rho imaging and the correction methods. Quantitative imaging in medicine and surgery. 2015;5(4):583-91

39. Raya JG, Dietrich O, Horng A, Weber J, Reiser MF, Glaser C. T2 measurement in articular cartilage: impact of the fitting method on accuracy and precision at low SNR. Magnetic resonance in medicine. 2010;63(1):181-93

40. Koff MF, Amrami KK, Felmlee JP, Kaufman KR. Bias of cartilage T2 values related to method of calculation. Magnetic resonance imaging. 2008;26(9):1236-43

41. Obuchowski NA, Mozley PD, Matthews D, Buckler A, Bullen J, Jackson E. Statistical Considerations for Planning Clinical Trials with Quantitative Imaging Biomarkers. Journal of the National Cancer Institute. 2019;111(1):19-26

42. Dixon WT, Oshinski JN, Trudeau JD, Arnold BC, Pettigrew RI. Myocardial suppression in vivo by spin locking with composite pulses. Magnetic resonance in medicine. 1996;36(1):90-4

43. Witschey WR, 2nd, Borthakur A, Elliott MA, Mellon E, Niyogi S, Wallman DJ, et al. Artifacts in T1 rho-weighted imaging: compensation for B(1) and B(0) field imperfections. Journal of magnetic resonance (San Diego, Calif : 1997). 2007;186(1):75-85

44.   Pang Y. A self-compensated spin-locking scheme for quantitative R(1ρ) dispersion MR imaging in ordered tissues. Magnetic resonance imaging. 2022;94:112-8

45.   Gram M, Seethaler M, Gensler D, Oberberger J, Jakob PM, Nordbeck P. Balanced spin-lock preparation for B(1) -insensitive and B(0) -insensitive quantification of the rotating frame relaxation time T(1ρ). Magnetic resonance in medicine. 2021;85(5):2771-80

46.   Mitrea BG, Krafft AJ, Song R, Loeffler RB, Hillenbrand CM. Paired self-compensated spin-lock preparation for improved T1ρ quantification. Journal of magnetic resonance (San Diego, Calif : 1997). 2016;268:49-57

47.   Chen W. Artifacts correction for T1rho imaging with constant amplitude spin-lock. Journal of magnetic resonance (San Diego, Calif : 1997). 2017;274:13-23

48.   Schuenke P, Koehler C, Korzowski A, Windschuh J, Bachert P, Ladd ME, et al. Adiabatically prepared spin-lock approach for T1ρ-based dynamic glucose enhanced MRI at ultrahigh fields. Magnetic resonance in medicine. 2017;78(1):215-25

49.   Gaj S, Yang M, Nakamura K, Li X. Automated cartilage and meniscus segmentation of knee MRI with conditional generative adversarial networks. Magnetic resonance in medicine. 2020;84(1):437-49

50.   Kim J, Mamoto K, Lartey R, Xu K, Nakamura K, Shin W, et al. Multi-vendor multi-site T(1ρ) and T(2) quantification of knee cartilage. Osteoarthritis and cartilage. 2020;28(12):1539-50

51.   Wang P, Block J, Gore JC. Chemical exchange in knee cartilage assessed by R1ρ (1/T1ρ) dispersion at 3T. Magnetic resonance imaging. 2015;33(1):38-42

52.　　Keenan KE, Ainslie M, Barker AJ, Boss MA, Cecil KM, Charles C, et al. Quantitative magnetic resonance imaging phantoms: A review and the need for a system phantom. Magnetic resonance in medicine. 2018;79(1):48-61

53.　　Chen CC, Wan YL, Wai YY, Liu HL. Quality assurance of clinical MRI scanners using ACR MRI phantom: preliminary results. Journal of digital imaging. 2004;17(4):279-84

54.　　Jiang Y, Ma D, Keenan KE, Stupic KF, Gulani V, Griswold MA. Repeatability of magnetic resonance fingerprinting T(1) and T(2) estimates assessed using the ISMRM/NIST MRI system phantom. Magnetic resonance in medicine. 2017;78(4):1452-7

55.　　Pruessmann KP, Weiger M, Scheidegger MB, Boesiger P. SENSE: sensitivity encoding for fast MRI. Magnetic resonance in medicine. 1999;42(5):952-62

56.　　Sodickson DK, Manning WJ. Simultaneous acquisition of spatial harmonics (SMASH): fast imaging with radiofrequency coil arrays. Magnetic resonance in medicine. 1997;38(4):591-603

57.　　Griswold MA, Jakob PM, Heidemann RM, Nittka M, Jellus V, Wang J, et al. Generalized autocalibrating partially parallel acquisitions (GRAPPA). Magnetic resonance in medicine. 2002;47(6):1202-10

58.　　Ying L, Liang Z-PJISPM. Parallel MRI using phased array coils. 2010;27(4):90-8

59.　　Li H, Yang M, Kim JH, Zhang C, Liu R, Huang P, et al. SuperMAP: Deep ultrafast MR relaxometry with joint spatiotemporal undersampling. Magnetic resonance in medicine. 2023;89(1):64-76

60. Wang Z, Arce GR. Variable density compressed image sampling. IEEE transactions on image processing : a publication of the IEEE Signal Processing Society. 2010;19(1):264-70

61. Levenberg K. A method for the solution of certain non-linear problems in least squares. Quarterly of applied mathematics. 1944;2(2):164-8

62. Marquardt DW. An algorithm for least-squares estimation of nonlinear parameters. Journal of the society for Industrial Applied Mathematics. 1963;11(2):431-41